Stepwise dual targeting and dual responsive polymer micelles for mitochondrion therapy

Xiaobin Zhang, Yi Wang, Guoqing Wei, Jingya Zhao, Guang Yang, Shaobing Zhou

PII: S0168-3659(20)30163-2

DOI: https://doi.org/10.1016/j.jconrel.2020.03.011

Reference: COREL 10213

To appear in: *Journal of Controlled Release*

Received date: 30 October 2019

Revised date: 24 February 2020

Accepted date: 7 March 2020

Please cite this article as: X. Zhang, Y. Wang, G. Wei, et al., Stepwise dual targeting and dual responsive polymer micelles for mitochondrion therapy, *Journal of Controlled Release* (2019), https://doi.org/10.1016/j.jconrel.2020.03.011

Stepwise dual targeting and dual responsive polymer micelles for mitochondrion therapy

Xiaobin Zhang[a,b,c‡], Yi Wang[a‡], Guoqing Wei[a], Jingya Zhao[a], Guang Yang[a] and Shaobing Zhou[a]*

[a] Key Laboratory of Advanced Technologies of Materials, Ministry of Education, School of Materials Science and Engineering, Southwest Jiaotong University, Chengdu, Sichuan 610031, P.R. China

[b] Radiation Chemistry Department, Sichuan Institute of Atomic Energy, Chengdu, Sichuan 610101, P.R. China

[c] Irradiation Preservation Key Laboratory of Sichuan Province, Chengdu, Sichuan 610101, P.R. China

* Corresponding author.
E-mail address: shaobingzhou@swjtu.edu.cn (S. Z.).

CRediT author statement

Xiaobin Zhang: Conceptualization, Methodology, Software **Xiaobin Zhang, Yi Wang**: Data curation, Investigation, Writing- Original draft preparation. **Guoqing Wei**: Visualization, Investigation. ***Jingya Zhao, Guang Yang:*** Investigation and Editing ***Shaobing Zhou:*** Writing- Reviewing and Editing

Abstracts

Methods to selectively destroy mitochondria of tumor cells and induce cell apoptosis with nanomedicine constitute challenges in cancer therapy. In the present study, we develop cell membrane/mitochondria dual targeting and pH/redox dual responsive nanoparticles for mitochondrion therapy. The nanoparticles are fabricated by the self-assembly of triphenylphosphonium (TPP) grafted poly(ethylene glycol)(PEG)-poly(d,l-lactide)(PLA) copolymers (TPP-PEG-ss-PLA) using disulfide bonds as the intermediate linkers. To shield the surface positive charge of the nanoparticles from TPP composition, chondroitin sulfate (CS) is employed to coat the nanoparticles, and this prolongs blood circulation while endowing an active targeting ability to the cell membrane. In acidic lyso-somes/endosomes, the negatively charged CS layer falls away to expose the TPP component. Subsequently, in the cyto-plasm, the nanoparticles can anchor to the mitochondrial outer membrane by TPP-mediated targeting, thereby inducing a decrease in the membrane potential and opening of the permeability transition pore. Thus, the overproduction of ROS in the mitochondria promotes cell apoptosis. The released DOX directly diffuse into the mitochondria, thereby resulting in mito-chondrial DNA damage. Therefore, the nanoparticles exhibit significant potential in terms of a new avenue for mitochondrion therapy in cancer treatment.

KEYWORDS: Mitochondrion therapy, dual targeting, micelle, drug delivery, nanoparticles

1. Introduction

A popular concept involves engineering nanoparticles to improve anticancer drug delivery and subsequent chemotherapy to malignant tumor. To achieve optimal delivery efficiency, nanoparticles should exhibit functions such as therapeutic targeting for cancerous organization, cell membranes, and subcellular organelles. The targeted delivery of a therapeutic agent to cancer tissues and cell membranes with nanoparticles is widely investigated [1-4].After the nanoparticles enter the cell, it is important for the carried cargos to reach specific organelles. The specific delivery of a therapeutic agent to molecular targets associated with certain organelles significantly improves drug action efficacy [5-8]. Therefore, increased research attention focuses on the organelle-specific targeting delivery of nanoparticles [9-11].

In a cell, the organelles mainly include nucleus, mitochondria, lysosomes, and ribosome. Specifically, mitochondria are the cell's powerhouse and maintain pivotal physiological functions [12-14], and also exert a lethal function via controlling the activation of an apoptotic effector in cancer cells [14, 15]. Additionally, the mitochondria also contains DNA. However, in contrast to nuclear DNA, introns are absent in mitochondrial DNA that only contains essential genes for the expression of mitochondrial proteins, tRNA, and rRNA [16]. Additionally, in the mitochondria, the DNA repair pathways are not processed, and this is different from that in the nucleus [17]. Thus, if the DNA-damaging anticancer drugs are delivered to the mitochondrial DNA, it presents increased advantages when compared to the method of targeting the nuclear genome.

However, targeting mitochondrial DNA is a process that is hard to achieve. The reason for this is mainly because mitochondrial membrane exhibits a typical thickness in which the outer and inner membranes have highly negative potentials ($\Delta\Psi$ = -150 to -180 mV) [18, 91], and the special hydrophobic and dense double-membrane structure acts as a formidable barrier to prevent bioactive compounds from gaining entry [16]. The DNA-damaging anticancer drugs cannot enter the mitochondria in which therapeutic effect is extremely limited. Therefore, to achieve a high therapeutic effect of mitochondrial DNA-damaging anticancer drugs, first, the drugs should precisely target mitochondria; and the permeability of mitochondrial membrane should be subsequently enhanced to allow the drugs to enter the mitochondria.

To selectively deliver a drug to the mitochondria, mitochondria-targeting signal peptides (MTSs) [20, 21], oligoguanidinium [22], and triphenylphosphonium (TPP) [23, 24] are widely employed to modify drug carriers in drug delivery systems. The ability to target mitochondria significantly improves the drug delivery efficacy of macromolecular carriers and widens the application of anticancer drugs [15]. Among these moieties for mitochondria targeting, TPP as a cation exhibits a unique chemical structure with lipophilicity and delocalized positive charge. It is selectively targeted to the mitochondria based on mitochondrial-membrane-potential-driven accumulation through the lipophilic phenyl groups and cationic phosphonium of TPP due to the negative potential gradient of the mitochondrion [15, 25].

To enhance the permeability of mitochondrial membrane and allow the therapeutic agents to enter mitochondria, a feasible method involves destroying the function of mitochondrial membrane. The damage to the mitochondria membrane affects the components of the mitochondrial respiratory chain and leads to the depolarization of mitochondria with a decrease in the mitochondria membrane potential ($\Delta\Psi$), thereby resulting in the opening of the permeability transition pore (PTP) of mitochondrial membrane and overproduction of the reactive oxygen species (ROS) [26, 27]. The functions of TPP possessing both mitochondrial targeting and mitochondrial damage are accepted [28-30]. Extant studies indicate that after anchoring in mitochondrial outer membrane, TPP makes the mitochondrial permeability transition, and this is also highly associated with the $\Delta\Psi$ [31]. However, the capacity to enhance the permeability of mitochondrial outer membrane is rarely examined.

As a concept of mitochondrion therapy, we synthesize a pH/redox dual responsive and cell membrane-/mitochondria- dual targeting nanoparticle that exhibits a significant capacity to inducing mitochondrial membrane depolarization to increase the permeability of mitochondrial membrane and allow therapeutic agents to enter mitochondria to cause mitochondrial DNA damage. As shown in **Scheme 1**A, the nanoparticles loaded with anticancer drug doxorubicin (DOX) are fabricated by the self-assembly of TPP grafted poly(ethylene glycol)(PEG)-poly(D, L-lactide) (PLA) copolymers using disulfide bonds as the intermediate linker (TPP-PEG-ss-PLA). To prolong the blood circulation and increase the endocytosis of tumor cells, the surface positive charges from TPP composition are transformed into negative charges via coating the nanoparticles with chondroitin sulfate (CS) (**Scheme 1**B). CD44 is a transmembrane glycoprotein which is overexpressed in most human cancers, including hepatoma carcinoma, breast cancer, ovarian cancer, squamous cell and so forth [32]. The CS layer as a CD44 acceptor also exhibits an ability to selectively mediate the endocytosis of the nanoparticles [33]. This would result in selective and preferential drug delivery to the tumor cells [34]. CS is hydrophilic and stable at pH 7.4 [35], it becomes hydrophobic when the pH decreases to 5.5 due to dissociation of carboxyl group [36, 37]. In lysosomes/endosomes, the negative charged CS layer is detached upon decreasing pH from 7.4 to 5.5, then falls off to expose the TPP due to the protonation of CS in acidic microenvironment, and surface charge reversal occurs on the nanoparticles. Subsequently, the nanoparticles target and anchor into mitochondrial outer membrane, thereby inducing the depolarization of mitochondrial membrane with decreases in the ΔΨ and increases in the mitochondria membrane permeability. Thus, the overproduction of ROS in mitochondria promotes cells apoptosis (**Scheme 1**C), and the released DOX from the disassembly of nanoparticles by glutathione (GSH) triggered redox-responsiveness directly diffuses into mitochondria since the membrane permeability increases. This results in mitochondrial DNA damage. Simultaneously, the other small part of the released DOX diffuses into nucleus, thereby leading to nuclear DNA damage. All the aforementioned actions promote the apoptosis of tumor cells.

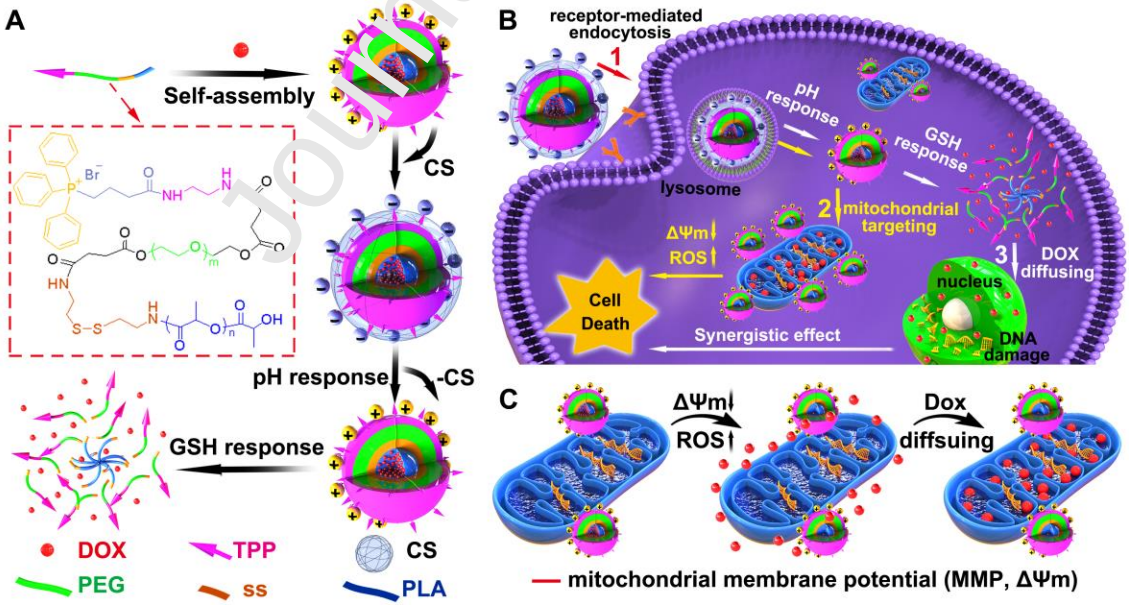

Scheme 1. A) Formation of the micelles by the self-assembly of TPP-PEG-ss-PLA polymer and subsequently coated with CS layer, and the disassembly of the nanoparticle via the initial deshielding of CS layer by pH-response followed by the cleavage of the disulfide bonds by GSH response. **B**) Schematic illustration of the stepwise dual targeting and dual response of the micelles to induce apoptosis of tumor

cells. 1) Increased endocytosis through receptor-mediated cell membrane targeting; 2) Mitochondrial targeting via TPP exposure due to pH response, which causes decreases in the membrane potential (ΔΨm) and overproduction of the ROS and finally leads to cell apoptosis; 3) The DOX released due to the disassembly by GSH response diffuses to the mitochondria and the nucleus and damages DNA. **C**) Magnification of the series process including mitochondrial targeting, decreases in the membrane potential (ΔΨm), overproduction of the ROS, and drug diffusion into the mitochondria.

2. Materials and Methods

2.1. Materials

Polyethylene glycol (PEG, Mw=2000) was purchased from Aldrich. D, L-lactide was prepared in our laboratory. 1-Ethyl-3-(3-dimethylaminopropyl)carbodiimide hydrochloride (EDC·HCl) , 4-(dimethylamino)pyridine (DMAP) and Carboxyl dextran (DEX, Mw=7000) were purchased from Biokem Chemical Reagent (Chengdu, China). JC-1 and 2,7-dichloro fluoresce in diacetate (DCFH-DA) were obtained from Aldrich Chemical Co. Triphenylphosphine and glutathione (GSH) were purchased from Adamas-beta Reagent, Ltd. (Shanghai, China). Bis(2-hydroxyethyl) Disulfide and Chondroitin sulfate sodium salt (CS, Mn=1526.03Da) was obtained from TCI (Shanghai) Development Co. Ltd. All other chemicals were purchased from Kelong Chemical Reagent Ltd.(Chengdu, China) and used without any treatments.

2.2. Cell Lines and Culture Conditions

Liver hepatocellular carcinoma (HepG2) were purchased from the Cell Bank of China Academy of Sciences (Shanghai, China). Cells were cultured in RPMI-1640 supplemented with 10% FBS fetal bovine serum (FBS) at 37 °C in a 5% CO_2 atmosphere and 100% humidity. Endothelial cells (EC) were obtained from Sichuan University (China). EC Cells were cultured in HyClone F12 supplemented with 10% fetal bovine serum (FBS).

2.3. Animals

Female Balb/c mice (18 ± 2 g) and female nude mice (20 ± 2 g) were feed at the condition of 25 °C and 55% of humidity and approved by the Institutional Animal Care and Use Committee of Sichuan University. All animal experiments were carried out in compliance with guidelines.

2.4 Synthesis of Boc-NH2

14 mL Ethylenediamine is dissolved into 200 mL dichloromethane (DCM), and the mixture is stirred at 0 °C to -5 °C. Additionally, 4.35 g $(Boc)_2O$ solution is added into 100 mL DCM, and the solution is then added dropwise to the reaction slowly within 6 h. It is reacted for another 24 h, and the reaction mixture is then filtered. The filtrate is washed with saturated salt water thrice, and the organic phase is separately concentrated under vacuum to yield a yellowish liquid (Boc-NH_2, yield: 81%).^{1}H NMR (400 MHz, $CDCl_3$) δ 5.64–5.40 (br, 1H, C(=O)-NH), 3.15–2.78 (m, 2H, $NHCH_2CH_2$, J = 5.8 Hz), 2.59 (t, J = 6.0 Hz, 2H, CH_2NH_2), 1.23 (s, 9H, t-Bu).

2.5. Synthesis of (3-Carboxypropyl)triphenylphosphonium bromide (TPP-COOH)

Triphenylphosphine (222 mg 0.16 mmol) and 4-Bromobutyric acid (70 mg 0.37 mmol) are dissolved in 100 mL N,N-dimethyl formamide (DMF). The mixture is kept stirring at 110 °C for 72 h, and the reaction mixture is then filtered to acquire white solid (TPP-COOH) (yield: 84%). ^{1}H NMR (400 MHz, DMSO-d6) δ 12.35 (s, 1H), 8.02–7.56 (m, 15H), 3.60 (td, J = 13.5, 7.7 Hz, 2H), 2.56–2.36 (m, 2H), 1.70 (td, J = 11.7, 9.7, 5.9 Hz, 2H).

2.6. Synthesis of Boc-TPP

Furthermore, Boc-NH_2 (1 g, 6.25 mmol), TPP-COOH (0.549 g, 1.28 mmol) and NHS (0.443 g, 3.85 mmol), and EDC·HCl (0.989 g, 5.16 mmol) are dissolved in 50 mL DMF, and EDC·HCl (0.989 g, 5.16 mmol) is added while stirring. The mixture is stirred at room-temperature until the Boc-NH_2 is completely reacted via monitoring with thin layer chromatography (TLC). When the reaction is complete, 5 mL deionized water is added and stirred for 30 min to quench the reaction. The solvent is removed in vacuo, and the residue is redissolved in 50 mL DCM and washed with 30 mL saturated salt water. The organic phase is dried by using anhydrous magnesium sulfate. After filtering the solid, the filtrate is condensed to obtain a pale yellow liquid (Boc-TPP, 73% yield).

2.7. Synthesis of COOH-PEG-COOH and Boc-NH-ss-NH_2

COOH-PEG-COOH and Boc-NH-ss-NH_2 are synthesized according to previously reported studies [38]. COOH-PEG-COOH: ^{1}H NMR (400 MHz, $CDCl_3$) δ 4.26 (br, 4H, -CH_2CH_2OCO-), 4.21–3.24 (m, 156H, -OCH_2CH_2O- and -C-(O)OCH_2CH_2-), 2.62 (br, 8H, -$CH_2CH_2C(O)OH$). Boc-NH-ss-NH_2: ^{1}H NMR (400 MHz, $CDCl_3$) δ 4.98 (s, ^{1}H, -C(O)NH-), 3.49 (q, J = 6.4 Hz, 2H, -C(O)$NHCH_2$-), 3.04 (t, J = 6.2 Hz, 2H, -CH_2NH_2), 2.89–2.70 (m, 4H, -CH_2ssCH_2-), 1.47 (s, 9H, t-Bu).

2.8. Synthesis of Boc-ss-PLA

The polymer is obtained via ring-opening polymerization of D, L- lactide with Boc-NH-ss-NH_2 as an initiator and $SnCl_2$ as a catalyst [39]. Briefly, 0.5 g Boc-NH-ss-NH_2, 12 g D,L-lactide, and 0.25 g of $SnCl_2$ are added to a 100 mL single neck bottle and vacuumed for 6 h. Then, the reaction was performed at 150 °C for 6 h. When the product is cooled to room-temperature, 2 mL DCM is added to dissolve the product into a paste, and this followed by a high amount of ice EtOH precipitation. The solid product is filtered and collected, and the white product Boc-ss-PLA is obtained by vacuum drying (Boc-ss-PLA, 81% yield).

2.9. Synthesis of PEG-ss-PLA

First, Boc-ss-PLA (4 g) is dissolved in 100 mL DCM, and 2 mL trifluoroacetic acid (TFA) is then added to the reaction while stirring. The reaction is subject to stirring at RM until the Boc-ss-PLA completely reacts under monitoring with TLC. Subsequently, the solvent is removed in vacuo, and the residue did not contain purified (PLA-ss-NH_2·TFA).

Second, COOH-PEG-COOH (2.2 g, 1 mmol) and DMAP（0.12 g, 1 mmol）are suspended in anhydrous DCM (150 mL). DCC (0.74 g, 3.6 mmol) is dissolved in DCM (50 mL), and the DCC solution is then added dropwise to the reaction. The mixture is stirred for 15 min, all the unpurified PLA-ss-NH_2 is then added, and the reaction mixture is stirred overnight at room temperature for 24 h. Subsequently, 5 mL deionized water is added and stirred for 30 min to quench the reaction. The reaction solution is filtered. The filtrate is concentrated under vacuum, and the residue is purified by re-crystallization from diethyl ether (PEG-ss-PLA, 60% yield).

2.10. Synthesis of TPP-PEG-ss-PLA and TPP-PEG-PLA

First, Boc-TPP (0.3 g, 0.53 mmol) is dissolved in 20 mL DMF, and 1 mL trifluoroacetic acid (TFA) is added to the reaction while stirring. The reaction is stirred at RM until the Boc-TPP reacts completely under monitoring with TLC. Subsequently, the solvent is removed in vacuo, and the residue is did not contain purified (TPP-NH_2·TFA).

Subsequently, PEG-ss-PLA (2 g, 0.32 mmol) and DMAP (1 g, 8.37 mmol) are added into DMF (50 mL). DCC (0.74 g, 3.60 mmol) is dissolved in DMF (20 mL) and added dropwise to the reaction. The mixture is stirred for 15 min, all the unpurified TPP-NH_2.TFA is then added, and the reaction mixture is stirred at room-temperature for 48 h. Furthermore, 5-mL deionized water is added and stirred for 30 min to quench the reaction. The reaction solution is filtered. The filtrate is concentrated under vacuum. The solvent is removed in vacuo, and the residue is purified via re-crystallization from diethyl ether. (TPP-PEG-ss-PLA, 68% yield).

In the same way, Boc-TPP (0.3 g, 0.53 mmol) is dissolved in 20 mL DMF, and 1 mL trifluoroacetic acid (TFA) is added. The solvent is removed in vacuo, and the residue does not contain purified (TPP-NH_2·TFA). PEG-PLA (2 g, 0.32 mmol) and DMAP (1 g, 8.37 mmol) are added into DMF (50 mL). DCC (0.74 g, 3.60 mmol) is dissolved in DMF (20 mL) and added dropwise to the reaction. The solvent is removed in vacuo, and the residue is purified via re-crystallization from diethyl ether. (TPP-PEG-PLA, 75% yield).

2.11. Micelles Formation

The micelles were prepared according to previous report with some change [40]. Briefly, 5 mg of TPP-PEG-ss-PLA was dissolved in 5 mL of THF. The TPP-PEG-ss-PLA solution was added dropwise into 10 mL of deionized water, the solution was allowed standing at 25 ℃ for 24 h under stirring. 1 mL of the CS water solution with 1 mg/mL was transferred into 10 mL TPP-PEG-ss-PLA solutions (1mg/mL) and the CS/TPP-PEG-ss-PLA nanoparticles were formed. DEX/TPP-PEG-ss-PLA nanoparticles were formed as same method. After the treatment of dialysis, the obtained water solution was lyophilized to provide the nanoparticles for the following experiments. The preparation process of CS/TPP-PEG-PLA@DOX, and CS/TPP-PEG-ss-PLA@DOX were slightly different from above. Take CS/TPP-PEG-PLA@DOX as example. First, DOX·HCl (1 mg) was dissolved in THF (10 mL), then a drop of triethylamine was added to remove hydrochloric acid and DOX was obtained. After that, the TPP-PEG-PLA (10 mg) was dissolved in the solution of DOX, the mixture was then added dropwise to deionized water (10 mL) under high-speed stirring. After THF was evaporated completely, the DOX-loaded micelles were transferred into dialysis bag (MWCO 1000) and dialyzed against deionized water to remove the unloaded DOX. After that, the obtained water solution was lyophilized to obtain the micelle. The freeze-dried micelle sample (TPP-PEG-PLA@DOX) was re-dissolved in water (1 mg mL^{-1}), 1 mL of the CS water solution with 1 mg/mL was transferred into 10 mL TPP-PEG-ss-PLA micelle solutions (the TPP-PEG-ss-PLA micelle solutions was obtained by resolving the freeze-dried micelle sample (TPP-PEG-PLA@DOX) into water (1 mg mL^{-1})) and the CS/TPP-PEG-PLA@DOX nanoparticles were formed.

2.12. Characterizations

In the present study, ^{1}H Nuclear Magnetic Resonance (^{1}H NMR) spectra were measured via the Bruker AM 300 apparatus. The solvents corresponded to $CDCl_3$ and $(CD_3)_2SO$, and the internal reference was Tetra-methylsilane (TMS). The average size and the Zeta potential of all the micelles were measured by dynamic light scattering (DLS) (Zeta-Sizer, Malvern Nano-ZS90, Malvern, U.K.). The morphology of micelles was detected by transmission electron microscopy (TEM) that consisted of a JEOL 2010F instrument (JEOL Ltd., Japan). Additionally, UV-vis spectrophotometer (UV-2550, Shimadzu, Japan) was used to detect the amount of DOX that was loaded in the polymer. The critical micelle concentration (CMC) was determined according to previous reports without changes by Fluoromax spectrometer (F-7000, Hitach, Japan) using pyrene as a florescent probe [41]. Samples for the TEM were prepared by drying a drop of the micellar solution (1 mg/mL) on a copper grid coated with amorphous carbon and staining with a drop of phosphotungstic acid solution (2 wt%). Drug-loading content (LC) and encapsulation efficiency (EE) of DOX-loaded micelles were determined by a UV-vis spectrophotometer (UV-2550, Shimadzu, Japan). The freeze-dried DOX-loaded micelle powders were re-dissolved in DMSO. The content of DOX in micelles was determined by measuring its absorbance at 488 nm using a pre-established calibration curve.

2.13. In vitro DOX Release

The *in vitro* DOX release was performed according to previous report with a slight change [42]. 10 mg of TPP-PEG-ss-PLA@DOX or TPP-PEG-PLA@DOX micelle powders were

dispersed in 10 mL PBS (pH 7.4) with 10 μM GSH, PBS (pH 7.4) with 10 mM GSH, disodium hydrogen phosphate-citric acid buffer (pH 5.0) with 10 μM GSH, or disodium hydrogen phosphate-citric acid buffer (pH 5.0) with 10 μM GSH in a dialysis bag (MWCO 1000). The dialysis bag was put into a tube which equipped with 30 mL corresponding medium and the bag was immersed in the incubation media. 1 mL of solution was removed at different time points (0, 3, 6, 9, 12, 24, 36, 48 and 72 h) for detected and replaced with 1 mL of fresh medium. The cumulative amount of released DOX from the micelles was detected by fluorescence spectrophotometer, and the percentages of released drug were plotted against time.

2.14. Cytocompatibility Assay

The cytocompatibility of blank micelles was evaluated by the Alamar Blue (AB) assay and live/dead staining which was performed according to previous report with slight change [3]. For the AB assay, 1×10^4 cells/well of HepG2 or HUVEC was seeded in 48-well plates. The PEG-ss-PLA and CS/TPP-PEG-ss-PLA with different concentrations (25, 50, 100, 200 and 400 μg/mL) were added to each well for 24 h, respectively. For live/dead staining, 2×10^4 cells/well of HepG2 or HUVEC was seeded in 24-well plates. The PEG-ss-PLA and CS/TPP-PEG-ss-PLA micelles with different concentrations (25, 50, 100, 200 and 400 μg/mL) were added to each well. The cytotoxicity study of free DOX, CS/TPP-ss-PLA nanoparticles and DOX-loaded micelles with HepG2 cells were also carried out with similar method as described above. The only difference was that the treated time was 48 h.

The cytotoxicity study of free DOX, CS/TPP-ss-PLA nanoparticles and DOX-loaded micelles were also carried out with similar method as described above, the DOX dosages varied from 0.075 to 5 μg/mL and the concentration of CS/TPP-ss-PLA nanoparticles varied from 15.6 to 1000 μg/mL. All groups were incubated with HepG2 for 48 h.

2.15. Flow Cytometry Studies

Flow cytometry was used to quantitatively evaluate the targeting effect of TPP. 1×10^5 cells/well of HepG2 cells were seeded in 6-well plates and cultured at 37 ℃ for 24 h. The free DOX and DOX-loaded micelles (DOX-equivalent dose: 5 μg/mL) were added and the cells continued to incubate for 3 h at 37 ℃. The culture medium was applied as a blank control. Cells were rinsed with PBS, harvested by trypsinization, centrifuged (1200 rpm, 4 min), and re-suspended in PBS. The DOX fluorescence intensity was measured by a FACS Calibur flow cytometer (BD Biosciences, U.S.A.).

2.16. In Vitro Cellular Uptake Studies

HepG2 cells were seeded in a confocal dish at a density of 5×10^4 cells/well and then cultured with free DOX and different DOX-loaded micelles for 3 h after that, the medium in the dishes was removed and the cells were washed with PBS for three times. Furthermore, the cells were fixed with 2.5% glutaraldehyde for 30 min and washed with PBS twice. Then the nuclei were stained with 4,6-diamidino-2-phenylindole (DAPI). Finally, the cells were the cells were observed by fluorescence microscopy (CKX41, Olympus, Japan).

2.17. The Mitochondrial Membrane Potential Analysis

Fluorescent probe JC-1 was employed to detect mitochondrial membrane potential changes using confocal laser scanning microscopic (CLSM) and flow cytometry. For CLSM, 1×10^5 cells/well of HepG2 cells were treated with PEG-ss-PLA and CS/TPP-PEG-ss-PLA micelles in 6-well plates for 6h, then the plates were washed three times with PBS. After that, the cells were incubated for 30 min with 1 μg/mL of JC-1 in culture medium at 37 ℃ in the dark. After 6 h incubation, the medium was removed and cells were washed with PBS for three times. The cells were examined by CLSM (TCS SP5, Germany), JC-1 green was excited at 529 nm

and the emission channel was set at 561 nm. Additionally, JC-1 red was excited at 490 nm, and the emission channel was set at 633 nm.

For flow cytometry, 1×10^5 cells/well of HepG2 cells were treated for 6 h, 12 h with PEG-ss-PLA and CS/TPP-PEG-ss-PLA micelles in 6-well plates, then the plates were washed three times with PBS. After that, the cells were detached with trypsin-EDTA solution. Collected cells were incubated for 30 min with 1 μg/mL of JC-1 in culture medium at 37 °C in the dark. And then, the cells were washed with PBS and analyzed by flow cytometer (BD Biosciences, U.S.A.).

2.18. The Measurement of Intracellular ROS Generation

The generation of intracellular ROS was measured via fluorescence microscopy using DCFH-DA as the sensor. For mitochondrial membrane potential measurements, the HepG2 cells were seeded in a 6-well plate at a density of 1×10^5 cells/well. After incubated for 24 h, PEG-ss-PLA and CS/TPP-PEG-ss-PLA micelles were added, then the cells were incubated for another predetermined time. DCFH-DA was added (final concentration 1×10^{-5} M) and the cells were incubated for 20 min. The cells were washed with PBS and then observed via fluorescence microscopy, repeatedly.

2.19. Cellular Uptake, Intracellular Distribution and Co-Location Analysis

To evaluate whether a variety of stimuli in cells can enhance release of DOX, the DOX-loaded DEX/TPP-PEG-ss-PLA and CS/TPP-PEG-ss-PLA micelles were incubated with HepG2 cells. The intracellular distribution of the DOX were observed via confocal laser scanning microscopic (CLSM). Briefly, HepG2 cells (1×10^5 cells per dish) were seeded in petri dishes (35 mm × 10 mm, Corning Inc., New York), after incubated for 24 h, the free DOX, CS/TPP-PEG-PLA@DOX and CS/TPP-PEG-ss-PLA@DOX micelles (DOX-equivalent dose: 5 μg/mL) were added. After 3 h incubation, the medium was removed and cells were washed with PBS for three times, then the mitochondria were stained with Mitotracker Green (Beyotime Biotech, China). Images were obtained using a Leica Microsystems CMS Gmbh (TCS SP5, Germany). DOX Emission of DOX moieties was observed using a 488 nm laser with the emission channel was set to be 570 nm and expressed as Red. Mitotracker Green was excited at 490 nm and the emission channel was set to be 516 nm. The amount of DOX in the cells and the Co-Location Analysis were finished by the Image Pro-Plus 6.0 Image J software.

2.20. In vivo Detection of Mitochondrial Membrane Potential and Generation of Tumor ROS

First, H22 (murine hepatic cancer cells) bearing Balb/c mice were i.v. injected with PEG-ss-PLA or CS/TPP-PEG-ss-PLA micelles. After 24 h, JC-1 or DCFH-DA probes were injected in situ. Approximately 0.5 h post-injection, the mice were anesthetized, and the tumor epidermis was cut with a scalpel and imaged via a two-photon confocal microscope (A1RMP Nikon). Subsequently, JC-1 green was excited at 529 nm and the emission channel was set at 561 nm. Additionally, JC-1 red was excited at 490 nm, and the emission channel was set at 633 nm; and DCFH-DA was excited at 529 nm and the emission channel was set at 561 nm. The amount of JC-1 and DCFH-DA fluorescence in the tumor were measured via Image Pro-Plus 6.0 software.

2.21. In vivo Antitumor Activity

H22 (murine hepatic cancer cells) bearing Balb/c mice were treated with saline, free DOX, DOX-loaded micelles (CS/TPP-PEG-ss-PLA, PEG-ss-PLA@DOX, CS/TPP-PEG-PLA@DOX and CS/TPP-PEG-ss-PLA@DOX) at a dosage of 5 mg DOX equiv./kg. A solution of 0.9% NaCl and CS/TPP-PEG-ss-PLA blank micelles were used as controls. The formulations were intravenously injected on days 0, 3 and 6. The tumor sizes were measured

every three days, and the volume was calculated according to the formula: $V = 0.5\times a \times b^2$, where a is the length of the tumor and b is the width of the tumor. The mice were weighed, and survival was recorded.

2.22. Histological Assessment

For the histological analysis (H&E and TUNEL staining), Balb/c mice were sacrificed at day 21 after the first treatment, and the tumors were collected and fixed in 10% formalin and embedded in paraffin blocks to prepare tumor sections at a thickness of 5 μm. After deparaffinization, the tissue sections were stained with hematoxylin and eosin (H&E) and terminal deoxynucleotidyltransferase mediated UTP end labeling (TUNEL) and were visualized by an optical microscope (Olympus, Japan).

2.23. Statistical Analysis

SPSS software was used for the statistical data analysis. Data were expressed as means ± SD. One way ANOVA was performed to determine statistical significance of the data. The differences were considered significant for p values ** < 0.01 *** < 0.001.

3. Results and discussion

3.1. Characterization of Polymer

The intermediates and the resultant TPP functionalized polymer TPP-PEG-ss-PLA are synthesized according to the routes shown in **Scheme S1** in Supporting Information (SI). First, the Boc-NH-ss-NH_2 intermediate is achieved in a manner similar to a method in a previous study [38], and the structure is confirmed by the ^{1}H nuclear magnetic resonance (^{1}H NMR) spectrum in **Figure S1** in SI. Subsequently, Boc-ss-PLA is obtained by the ring-opening polymerization of D, L-lactide using Boc-NH-ss-NH_2 as an initiator, and its structure and molecular weight (Mn = 5030 Da) are determined with ^{1}H NMR (**Figure S2** in SI). Finally, a series of condensation reactions is used, and the resultant polymer TPP-PEG-ss-PLA is obtained. The intermediates (**Figure S3–S7**) and TPP-PEG-ss-PLA with Mn = 7500 Da (**Figure S8**) are characterized by ^{1}H NMR to confirm the structures and compositions. As shown in in **Figure S8**, we clearly observe peaks for the characteristic groups of the aromatic ring group of the TPP (8.06–7.65 ppm), methylene group of the PEG (3.32 ppm), and methyl group of the PLA component (1.45 ppm), thereby indicating that TPP-PEG-ss-PLA is successfully synthesized.

3.2. Characterization of the Micelle

The micelle is obtained by the self-assembly of amphiphilic TPP-PEG-ss-PLA polymer. As shown in the transmission electron microscopy (TEM) images and particle size distribution determined by the dynamic laser scattering (DLS) method, it is clearly observed that the TPP-PEG-ss-PLA blank micelles exhibit a well spherical shape, average size of 101.5 nm with a nearly uniform distribution, and positive zeta potential of +20.8 mV (**Figures 1A** and **1B** and **Table S1** in SI). To avoid elimination by the reticuloendothelial system (RES) in the blood circulation, the CS are wrapped around the surface of micelles to reverse their positive charge by electrostatic adsorption. Following the CS coating, the morphology of the CS/TPP-PEG-ss-PLA micelles is still maintained as spherical, the size slightly increases to 135.0 nm; and the zeta potential is fully reversed to -21.4 mV (**Figure 1C** and **1D**). When the anticancer drug DOX is encapsulated in the micelles, the shape, size, and zeta potential are almost unchanged. The drug-loading content (LC) and encapsulation efficiency (EE) of all the micelles approximately correspond to 6.0% and 70%, respectively (**Table S1**). The other micelles including PEG-ss-PLA, TPP-PEG-PLA, and DOX loaded micelles are also prepared as controls and their properties are also summarized in **Table S1**.

3.3. pH and Redox Responsive Abilities

To demonstrate whether the CS/TPP-PEG-ss-PLA micelles drop off the CS layer via pH responsiveness and regain mitochondrial targeting function after they enter tumor cells, we measure the changes in both the particle size and zeta potential by varying pH values from 7.4 to 4.5. As shown in **Figure 1G**, the particle size and zeta potential do not significantly change when the pH is adjusted from 7.4 to 6.5. When the pH is adjusted to 5.5, the particle size reduces to ~100 nm; and the zeta potential reverses from -20 mV to +20 mV. To further verify the pH sensitivity of CS/TPP-PEG-ss-PLA micelles, we investigate changes in the particle size and potential with respect to time at pH 5.5. The results in **Figure 1H** indicate that the surface charge of the CS/TPP-PEG-ss-PLA micelles reverse from negative to positive in less than 5 minutes, and the micellar size changes similarly. This indicates that the shedding of CS layer occurs immediately to expose TPP moieties in an acidic microenvironment. Additionally, the introduction of disulfide bond as links between hydrophilic and hydrophobic segments in TPP-PEG-ss-PLA polymer endows the micelles with redox-sensitivity in a high concentration of glutathione (GSH) in the cytoplasm of tumor cells [41-43]. Therefore, the redox-responsiveness of the micelles is also measured in a simulated cytoplasmic environment (pH 7.4 and GSH 10 mM). As shown in **Figures 1E** and **1F**, a few large aggregates are formed, and the size of TPP-PEG-ss-PLA micelles gradually changes from 101.5 nm to exceed 1000 nm in 24 h. The high redox-responsiveness accelerates the release of the encapsulated DOX from the micelles. The *in vitro* DOX release profiles are shown in **Figure 1I** and indicate that the cumulative release of DOX reaches ~84.1% in 72 h following the treatment of the PEG-ss-PLA@DOX micelles by pH 7.4 and GSH 10 mM while the cumulative release of DOX only reaches ~30% at pH 7.4 and GSH 10 μM. This is similar to a normal physiological condition. The result observed that the micelles prevent the therapeutic agent from leaking in blood circulation and also realize rapid drug release in tumor cells. Additionally, the cumulative release of DOX from PEG-PLA@DOX micelles without disulfide bonds is significantly lower in the simulated cytoplasmic microenvironment.

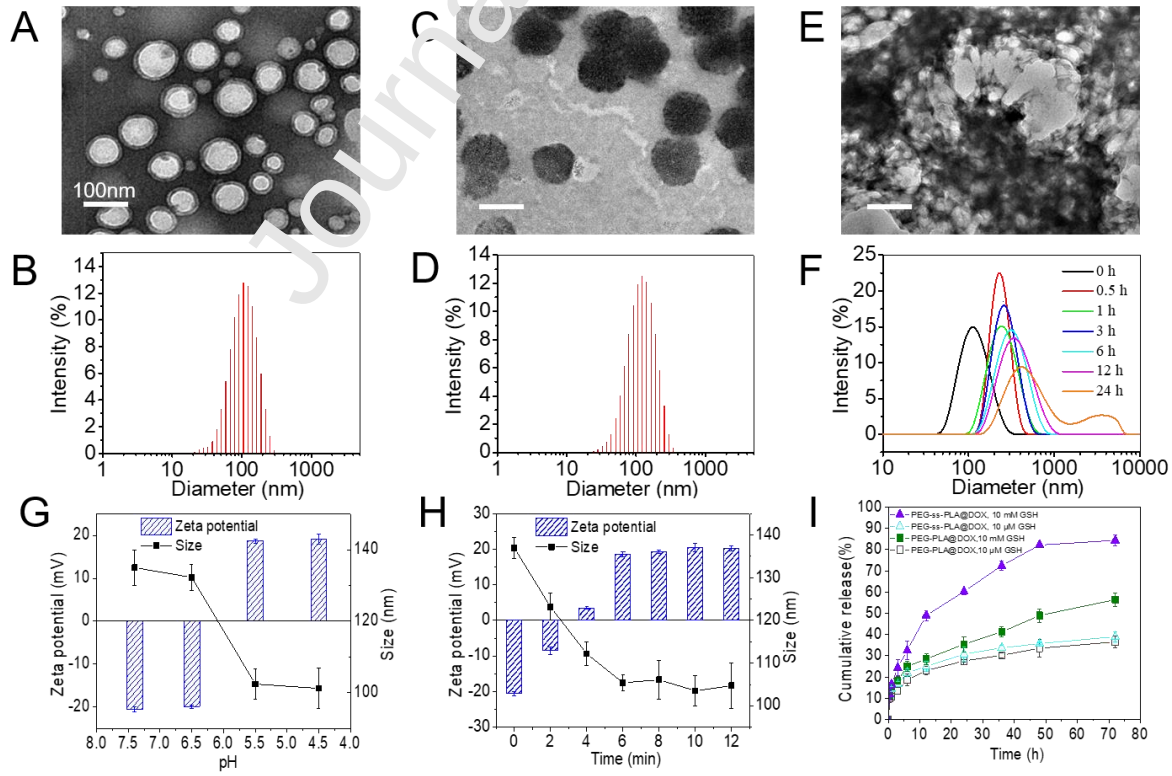

Figure 1. Determination of the pH and reduction in the sensitivity of the micelles. Transmission electron microscopy (TEM) images and changes in the size of corresponding nanoparticles: **A-B**) TPP-PEG-ss-PLA; **C-D**) CS/TPP-PEG-ss-PLA; **E-F**) Morphology and size changes for CS/TPP-PEG-ss-PLA nanoparticles in 10 mM GSH at pH 7.4; **G-H**) Determination of pH sensitivity of the CS/TPP-PEG-ss-PLA nanoparticles for different pH values and times (indicates ± standard deviation (SD), n = 3); **I**) *In vitro* DOX release profiles (indicates ± SD, n = 3).

3.4. Cell Membrane Targeting

To verify whether the CS layer as a CD44 acceptor targets the cell membrane and enhances the endocytosis of the nanoparticles, confocal laser scanning microscope (CLSM) is employed to visualize the HepG2 cells following incubation with saline, free DOX, different DOX-loaded nanoparticles, and CS coated DOX-loaded nanoparticles. Dextran (DEX) does not actively target tumor cells overexpressed CD44 receptors and instead exhibits excellent biocompatibility. It is selected as a control for coating TPP-PEG-ss-PLA@DOX micelles. As shown in **Figure S9**, the cells are treated by DEX coated nanoparticles and the red fluorescence is extremely weak, thereby implying that only a low number of nanoparticles are internalized due to the lack of cell membrane targeting. In the CS/TPP-PEG-ss-PLA@DOX group, a significantly stronger red fluorescence is observed, thereby suggesting that additional micelles are internalized via the receptor-mediated targeting effect. The flow cytometry analysis shown in **Figure S10** indicates a high degree of agreement. Additionally, we evaluate the cytotoxicity of the blank micelles. The viability of HepG2 cells is investigated by Alamar Blue (AB) assay and live/dead staining following incubation with the micelles with different concentrations for 24 h. As shown in the fluorescence images in **Figure S11** and AB results in **Figure S12**, when the concentration of the micelles increases to 200 μg/mL, the cells grow in a healthy manner, and a few dead cells are observed. The cell viability still exceeds 85%. The cell viability slightly decreased to ~80% when the concentration of the CS/TPP-PEG-ss-PLA micelles reaches 400 μg/mL, thereby indicating that the blank micelles exhibit inhibited effect on tumor cell growth, and this is potentially because the TPP target the mitochondria and induce the depolarization of the mitochondrial membrane.

3.5. Mitochondria-Targeting Ability

To investigate the mitochondria-targeting efficiency, we compare the behavior of corresponding DOX-loaded nanoparticles with confocal laser scanning microscope (CLSM) via co-localization analysis. The groups are adopted and include free DOX, CS/TPP-PEG-PLA@DOX without redox-responsiveness, and CS/TPP-PEG-ss-PLA@DOX with redox-responsiveness. In the CLSM images (**Figure 2**A), the mitochondria of HepG2 cells are specially stained to green color with Mito traker green (MTG) dye, and DOX exhibits red fluorescence. When DOX and mitochondria overlaps, yellow fluorescence appears due to the merging of green and red colors. In the free DOX group, the green and red colors are distinctively separated and located in the mitochondria and nucleus, respectively, thereby suggesting that free DOX does not enter the mitochondria and instead diffuses into the nucleus. The encapsulated DOX in the micelles are released rapidly because the micelles are disassembled through the cleavage of the disulfide bonds in the micelle matrix under a high GSH level in cytoplasm [44, 45]. The released DOX in cytoplasm diffuses into other organelles. In the TPP functionalized micelle groups (CS/TPP-PEG-PLA@DOX, CS/TPP-PEG-ss-PLA@DOX), yellow fluorescence is observed in the mitochondria in the merged images, thereby indicating a good overlap between the green color for mitochondria and the red color for DOX. Furthermore, only a low amount of red fluorescence is observed in the

nucleus, thereby suggesting that only a low amount of DOX diffuses into the nucleus. Additionally, the corresponding linear regions of interest intensity profiles across the white line (marked in the CLSM images) are also employed to demonstrate the DOX distribution. As shown in **Figure 2B**, the green and red peaks denote the mitochondria and DOX, respectively. In a manner similar to the result in **Figure 2A**, only in TPP functionalized micelle groups, green and red peaks completely overlap in the region of mitochondria, and a few red peaks are obtained in the area of nucleus. The results also demonstrate that the CS layer of the micelles is effectively removed, and the exposed TPP moieties in turn possess excellent mitochondria- targeting ability, thereby leading to a specific accumulation of nanocarriers at the mitochondrial region and lead to an improvement in the membrane permeability of mitochondria and finally result in the direct diffusion of the released DOX into mitochondria.

To quantitatively evaluate the DOX distribution in organelles, Pearson's correlation (Rr) and overlap coefficient (R) are utilized to demonstrate the correlation of two types of fluorescence based on the fluorescence co-localization analysis. When the Rr value is closer to 1, it indicates that the co-location of two types of fluorescence improves [46]. Additionally, R is typically used to describe the degree of overlap between two types of fluorescence. The R value ranges from 0 to 1 and increases in the R value increase the co-localization area [47]. As shown in **Figure 2C**, the green and red colors also denote the fluorescence of mitochondria and DOX, respectively. When compared to the free DOX group (Rr =0.67, R =0.68), the CS/TPP-PEG-PLA@DOX group exhibits increased Rr (0.97) and R (0.97), and this indicates that it can accurately target the mitochondria and release the DOX into the mitochondria. The Rr and R values of CS/TPP-PEG-ss-PLA@DOX are 0.92 and 0.93, respectively, and this also demonstrates the function. The Rr and R values of CS/TPP-PEG-ss-PLA@DOX are slightly lower than those of CS/TPP-PEG-PLA@DOX. The reason is potentially because a part of DOX is released in cytoplasm and diffused into nucleus due to the disassembly of nanoparticles via the redox-responsiveness before the CS/TPP-PEG-ss-PLA@DOX targets the mitochondria, which also means the DOX amount that can be delivered by the nanoparticles into the mitochondria will be decreased. Simultaneously, the other small part of the released DOX diffuses into nucleus, thereby leading to nuclear DNA damage. All the aforementioned actions promote the apoptosis of tumor cells. Thus, all the results indicated that the TPP functionalized micelles possess the capacity to target mitochondria and improve membrane permeability, thereby leading to the direct diffusion of the released DOX into the mitochondria.

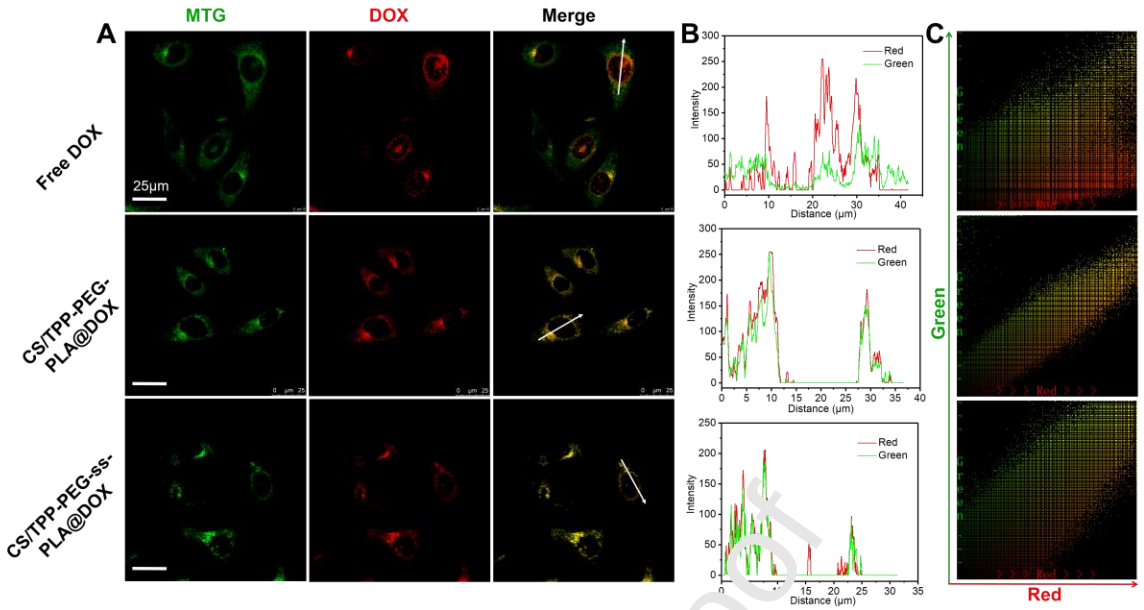

Figure 2. Mitochondria-targeting analysis. **A**) CLSM images for tracking DOX delivery in HepG2 cells with MitoTracker-stained mitochondrion channel (green) or DOX channel (red). **B, C**) Co-localization analysis.

3.6. Mitochondrial Membrane Potential Analysis

To determine whether the mitochondrial membrane potential decreases and leads to improvements in the membrane permeability, a fluorescent probe, 5,5',6,6'-tetrachloro-1,1',3,3'-tetraethylbenzimidazolcarbocyanine iodide (JC-1), was employed. It is capable of selectively entering mitochondria since it changes its color from red to green when the membrane potential decreases [48, 49]. The normal mitochondria are accompanied by the red fluorescence emission due to the formation of J-aggregates while the depolarized mitochondria display green fluorescence due to the formation of J-monomers [50]. Thus, changes in the membrane potential is measured by detecting the green/red fluorescence intensity ratio. As shown in **Figure 3A**, the HepG2 cells treated with the micelles without TPP targeting for 6 h still display red fluorescence, thereby suggesting that the mitochondrial membrane potential is almost maintained as unchanged. Conversely, the cells treated with CS/TPP-PEG-ss-PLA micelles gradually exhibit green fluorescence, and the red fluorescence decreases or disappears, thereby implying decreases in the membrane potential. Flow cytometry studies also confirmed that when the HepG2 cells are incubated with the CS/TPP-PEG-ss-PLA micelles, the decrease in red fluorescence is evident and time-dependent (**Figures 3B–D**). The ratio of the green to red fluorescence increase with increases in both the incubation time and micelle concentration, and this also demonstrates that the TPP functionalized micelle possesses the ability to decrease the mitochondrial membrane potential (**Figure S13**). Thus, it increases the permeability of the mitochondrial membrane [51].

3.7. ROS Generation

When the permeability of mitochondrial membrane increases, the ROS is generated and enters the cytoplasm [52]. Thus, we further examine whether the ROS is produced when the TPP functionalized nanoparticles act on the mitochondria of cancer cells. The fluorescence probe, 2',7'-Dichlorodihydrofluorescein diacetate (DCFH-DA), is employed to measure the generated ROS. The DCFH-DA is oxidized by ROS and in turn produces green fluorescence. As shown in **Figure 3E**, after an incubation period of 6 h, a significantly stronger green

fluorescence is clearly observed in the CS/TPP-PEG-ss-PLA group in contrast to the group without TPP targeting, thereby indicating that several ROS are generated. Furthermore, as shown in the quantitative result of the fluorescence intensity in **Figure 3F**, the intensity of the mitochondria-targeted CS/TPP-PEG-ss-PLA is approximately thrice that without TPP target, thereby suggesting that the cells increase ROS due to increases in the mitochondrial membrane permeability. Additionally, with increases in the CS/TPP-PEG-ss-PLA concentration, the green fluorescence intensity also increases (**Figure 3G**), thereby indicating that the ROS generation in cytoplasm is concentration-dependent. The results also confirm the improvement in mitochondrial membrane permeability. The IC_{50} value is the concentration that results in 50% cell inhibition, and it is employed to evaluate the antitumor efficacy. As shown in **Figure 3H** and **Table S2**, the blank CS/TPP-PEG-ss-PLA micelles display a IC_{50} value similar to that of the DOX-loaded PEG-PLA micelles. Thus, the blank material exhibits a certain amount of cytotoxicity to tumor cells. The result is ascribed to the fact that the generated ROS results from TPP-induced mitochondrial membrane destruction and causes cell apoptosis. Furthermore, the DOX-loaded CS/TPP-PEG-ss-PLA micelles exhibit an extremely low IC_{50} value, thereby implying that a synergistic effect of the released DOX exists and leads to mitochondrial DNA damage and generates ROS function on cell apoptosis. At the same time, CS/TPP-PEG-PLA/DOX micelles exhibited a slightly higher IC50 than CS/TPP-PEG-ss-PLA/DOX micelles, which was due to the cleavage of the disulfide bond, and more DOX was released. It means the DOX amount that can be delivered by the micelles into the mitochondria will be decreased. Simultaneously, the other small part of the released DOX diffuses into nucleus, thereby leading to nuclear DNA damage. All the aforementioned actions promote the apoptosis of tumor cells.

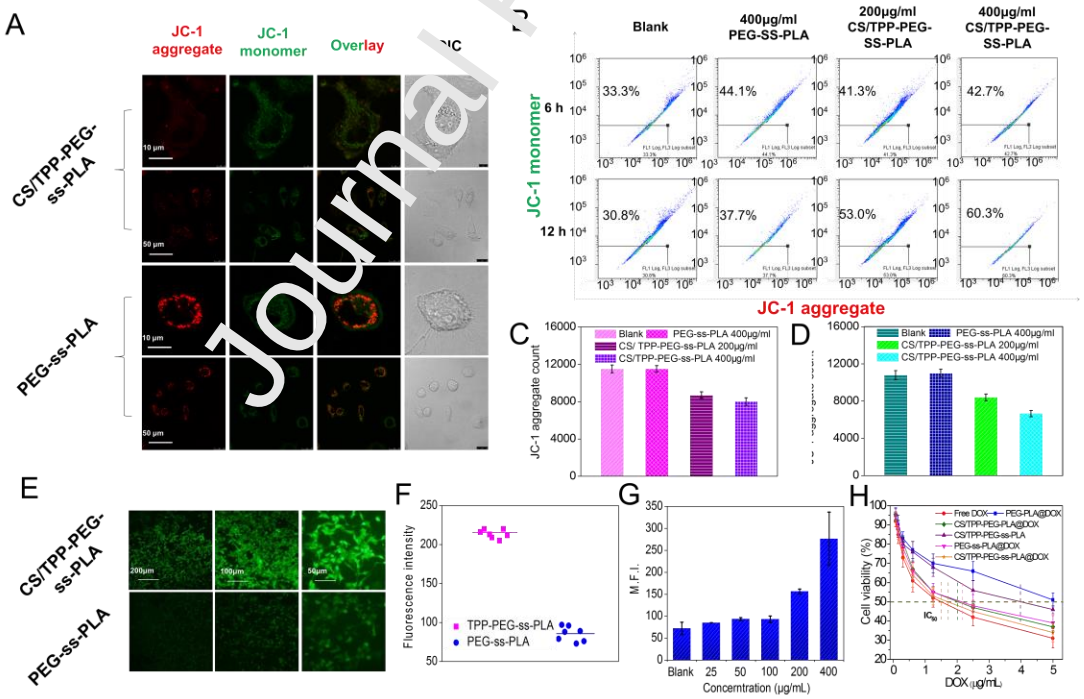

Figure 3. *In vitro* Analyses of the mitochondrial membrane potential and ROS generation. **A**) JC-1 staining in HepG2 cells via treatment with different micelles for 6 h. **B**) Flow cytometric analyses of mitochondrial membrane potential using JC-1 as indicator for HepG2 cells treated with various micelles at different concentrations for 6 h and 12 h. Relative intensity of JC-1 red fluorescence for **C**) 6 h and **D**) 12 h (indicates ± SD, n = 3). **E**) DCFH-DA staining in HepG2 cells after treatment with different micelles for 6

h. **F**) Relative intensity of DCFH-DA green fluorescence. **G**) Mean fluorescence intensity (MFI) of the DCFH-DA staining in HepG2 cells after treatment with CS/TPP-PEG-ss-PLA at different concentrations (indicates ± SD, n = 3). **H**) Viability of HepG2 cells following incubation with free DOX and DOX-loaded corresponding nanoparticles (indicates ± SD, n = 3).

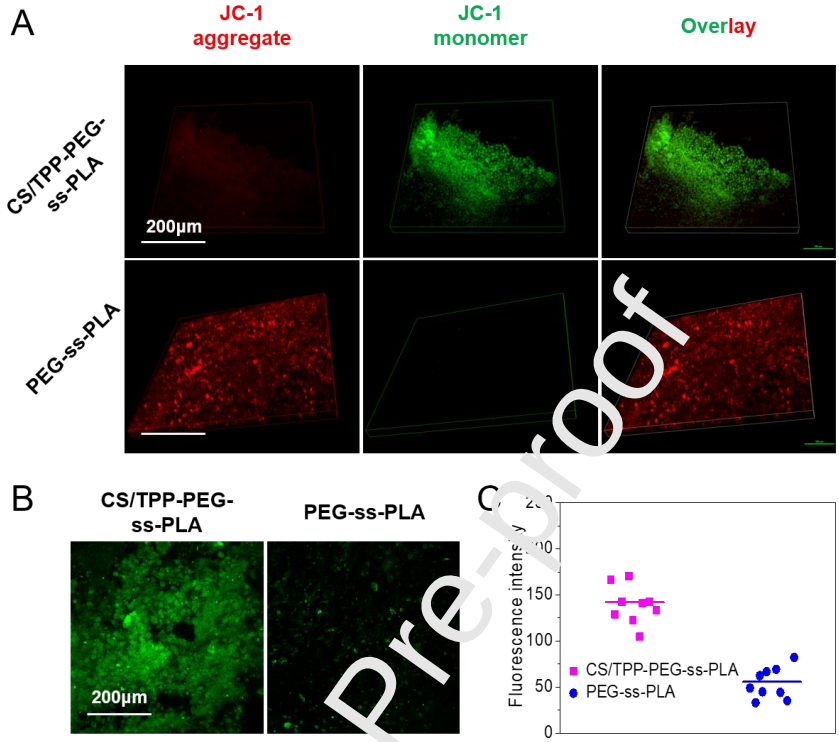

Figure 4. *In vivo* analysis of mitochondrial membrane potential and ROS generation. Two-photon laser confocal fluorescence microscopy images of **A**) in vivo JC-1 staining and **B**) DCFH-DA staining on Balb/c mice bearing H22 tumor following treatment with different micelles for 24 h. **C**) Relative intensity of DCFH-DA fluorescence from green.

3.8. In vivo Analysis of Mitochondrial Membrane Potential and ROS Generation

To verify whether the TPP modified nanoparticles decrease mitochondrial membrane potentials and ROS generation *in vivo*, we intravenously injected the nanoparticles without DOX on Balb/c mice bearing murine hepatic cancer (H22). At 24 h after injection, JC-1 or DCFH-DA fluorescent probes are intravenously injected on the mice [53, 54]. As shown in the two-photon laser confocal fluorescence microscopy images in **Figure 4A**, the tumor tissue treated PEG-ss-PLA micelles without TPP targeting maintain the red fluorescence of JC-1 aggregates. However, the tumor treated with CS/TPP-PEG-ss-PLA micelles display the green fluorescence of JC-1 monomers. The *in vivo* result is consistent with the *in vitro* data in **Figures 3A** and **3B**. It also observed that the TPP functionalized nanoparticles decrease the mitochondrial membrane potential. Subsequently, we investigate the intracellular ROS generation in tumor tissue by injection of DCFH-DA probe. As shown in **Figure 4B**, significantly stronger green fluorescence in tumor treated with the CS/TPP-PEG-ss-PLA is observed when compared with that without TPP targeting. Furthermore, the mean fluorescence intensity indicates a significant difference between the CS/TPP-PEG-ss-PLA and PEG-ss-PLA groups (**Figure 4C**), and this is in good agreement with the *in vitro* result in **Figures 3E–G**. The result also suggests that the mitochondrial membrane potentials decrease and the ROS is definitely generated in cytoplasm.

3.9. In vivo Fluorescence Image

To further verify the cell membrane- targeting and redox-responsive capacities *in vivo*, we inject the micelles on H22 tumor bearing nude mice, and monitor the fluorescence of DOX at different time points. As shown in **Figure 5A**, in contrast to DEX/TPP-PEG-ss-PLA@DOX group without active targeting, CS/TPP-PEG-ss-PLA@DOX group display stronger DOX fluorescence in the tumor, thereby indicating the increased accumulation of the micelles. Additionally, the DOX concentrations in the collected plasma and main organs including heart, liver, spleen, lung, kidney, and tumor tissues at predesigned time points are measured via fluorescence spectroscopy. The pharmacokinetic profiles of the DOX formulations are shown in **Figure 5B**. As shown in the figure, in contrast to the free DOX, the elimination of DOX from the blood is slower after it is encapsulated in micelles. Specifically, when the micelles are coated by CS layer, the blood circulation time is significantly prolonged and increases to ~20 h. Biodistributions of DOX in main organs and tumor tissues versus time are shown in **Figure 5C–H**. The DOX is typically accumulated in tumor, liver, heart, spleen, lung, and kidneys at each time point. However, in contrast to the free DOX, other DOX nano-formulations presented increased accumulation in tumor tissues. Furthermore, the accumulation increases with increases in time. Specifically, the DOX accumulation of the CS coated DOX-loaded micelles significantly increases and reaches ~7.5% at 24 h. This is ~1.7 times that of PEG-ss-PLA@DOX group without active targeting and ~9 times that of the free DOX. All the results indicate that the CS coated micelles also exhibit excellent active targeting ability.

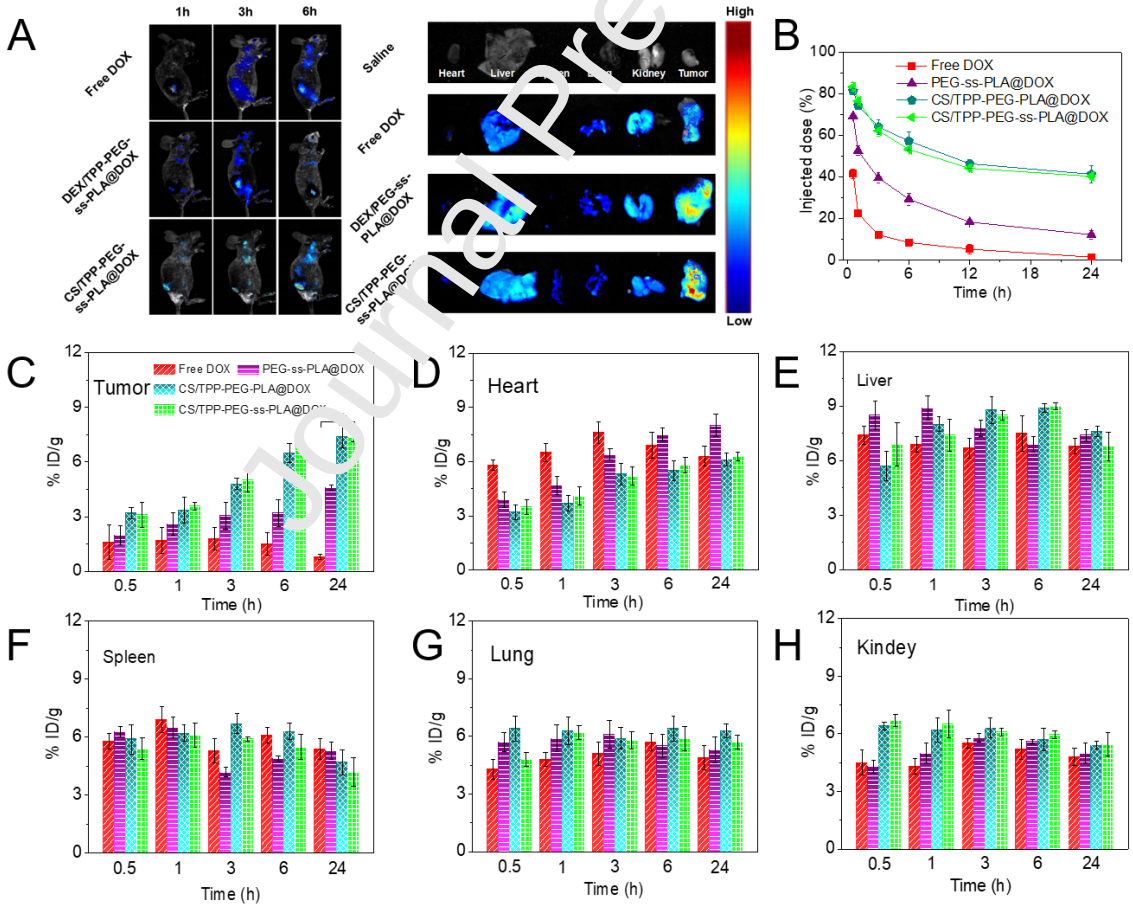

Figure 5. *In vivo* and *ex vivo* biodistribution analyses. **A)** *In vivo* fluorescence images of H22 tumor bearing nude mice following intravenous injection of various DOX formulations and *ex vivo* fluorescence images of isolated tissues at 6 h post-injection. **B)** Pharmacokinetic profiles of total DOX, post-intravenous

injection of various DOX formulations (indicates ± SD, n = 3). **C-H**) DOX distribution in the tumor, heart, liver, spleen, lung, and kidneys (n = 3) (dose: 2 mg DOX/kg body weight, indicates ± SD, **P < 0.01).

3.10. In vivo Antitumor Efficacy

To establish the clinical translation potential of DOX-loaded nanoparticles, we perform therapeutic studies via injecting nanoformulations on H22 tumor bearing Balb/c mice. The antitumor efficacy is shown in **Figure 6**. As shown in **Figures 6A** and **B**, the mean tumor volume continuously increases to ~1200 mm^3, 700 mm^3, 422 mm^3, and 400 mm^3 following 21-d treatment with saline, PEG-ss-PLA@DOX, free DOX, and blank CS/TPP-PEG-ss-PLA, respectively. However, the tumor growth is significantly inhibited via treatments of the DOX-loaded TPP functionalized micelles. Specifically, the tumor volume in the CS/TPP-PEG-ss-PLA@DOX group was only ~101 mm^3, and this was only half that in CS/TPP-PEG-PLA@DOX group. This result also indicates that the disulfide bonds can increase the release of DOX, increasing the antitumor effect of DOX-loaded TPP functionalized micelles. It should be noted that the blank CS/TPP-PEG-ss-PLA micelles represent comparative antitumor efficacy, which is similar to that of the free DOX. This is also in accordance with the *in vitro* antitumor effect with IC_{50} value of ~4 μg/mL DOX equivalent (**Figure 3H**). The reason is mainly attributed to the fact that the TPP target mitochondria and the depolarization of the mitochondrial membrane of tumor cells. The inhibition rate of tumor growth is approximately 60% in CS/TPP-PEG-ss-PLA group and 90% in CS/TPP-PEG-ss-PLA@DOX group (**Figure 6D**). The results indicate that the blank material CS/TPP-PEG-ss-PLA possess a certain therapeutic effect by mitochondrial damage. Furthermore, the antitumor efficacy further enhances significantly following the combination of DOX into the material. This suggests the synergistic effect of the chemotherapy of DOX-inducing DNA damage and the mitochondrial damage. The antitumor efficacy is further confirmed via a histological evaluation of tumor tissues stained with hematoxylin and eosin (H&E) and terminal deoxynucleotidyl transferase-mediated dUTP end labeling (TUNEL). The apoptosis of tumor cells is caused by the nanoparticles also can be clearly confirmed through TUNEL and H&E analyses of tumor sections after treatment *in vivo*. **Figure 6E** shows extensive nuclear shrinkage and fragmentation and massive tumor necrosis in the CS/TPP-PEG-ss-PLA@DOX group, and this further indicates the optimal antitumor efficacy. Additionally, an evident decrease in body weight is absent in all the groups with the exception of the free DOX group (**Figure 6C**), thereby suggesting that the nanomedicines exhibit almost no systemic toxicity, and the side effect of free DOX is overcome via the encapsulation of the materials.

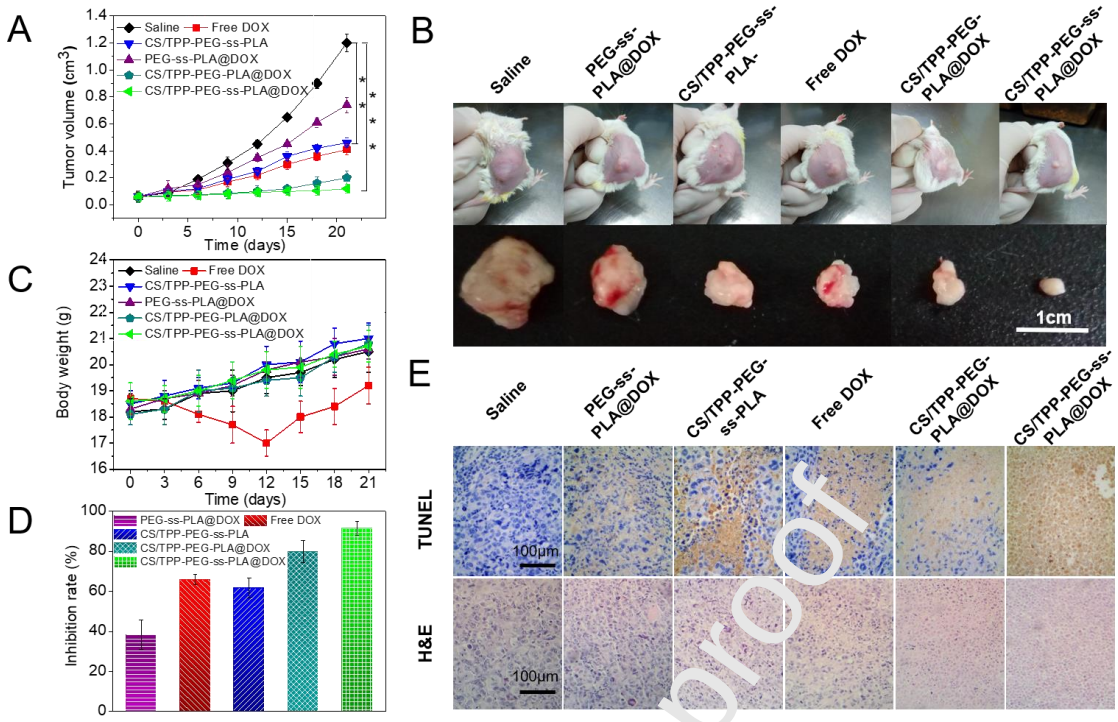

Figure 6. *In vivo* antitumor activity evaluation. **A**) Changes in the tumor volume and **B**) Monitored tumor size of Balb/c mice bearing H22 tumor following intravenous saline injection, DOX·HCl, and corresponding nanoparticles (2.0 mg DOX/kg body weight, indicates ± SD, n = 7), **C**) Body weight, **D**) Tumor growth inhibition, **E**) TUNEL and H&E analyses of tumor sections after treatment. In TUNEL staining, normal cells are stained blue, and apoptotic cells are stained brown. In H&E staining, nuclei are stained blue, and the extracellular matrix and cytoplasm are stained red. (**P < 0.01 and ***P < 0.001)

4. Conclusions

In summary, we presented a cell membrane/mitochondria dual targeting and pH/redox dual responsive nanoparticle. The nanoparticle exhibits a long blood circulation time due to the negative charged surface and enhanced specific internalization of tumor cells. In lysosomes/endosomes, the negative charged CS layer falls off to expose the TPP in response to the acidic microenvironment, and the nanoparticle targets and anchors into mitochondrial outer membrane, thereby inducing the depolarization of mitochondrial membrane with decreases in the ΔΨ and increases in the mitochondria membrane permeability. Thus, the overproduction of ROS in mitochondria promotes cell apoptosis, and the released DOX from the disassembly of nanoparticles directly diffuses into mitochondria, thereby resulting in mitochondrial DNA damage. All the aforementioned actions prompt the apoptosis of tumor cells. Therefore, this work provides a new strategy for the design and engineering of a smart nanoplatform for the mitochondrion therapy of malignant tumors.

Acknowledgements

This work was partially supported by the China National Funds for Distinguished Young Scientists (51725303), the National Natural Science Foundation of China (21574105, 51603172, 81701831) and the Sichuan Province Youth Science and Technology Innovation Team (Grant No.2016TD0026).

Appendix A. Supplementary data

Supplementary data related to this article can be found online at http://xxxxxxxxxxxx.

Data availability statement

All data included in this study are available upon request by contact with the corresponding author.

References

[1] R. Langer, New methods of drug delivery, Science 249 (1990) 1527-1533.
[2] X. Guo, L. Wang, K. Duval, J. Fan, S. Zhou, Z. Chen, Dimeric drug polymeric micelles with acid-active tumor targeting and FRET-traceable drug release, Adv. Mater. 30 (2018) 1705436.
[3] Y. Wang, G. Wei, X. Zhang, F. Xu, X. Xiong, S. Zhou, A step-by-step multiple stimuli-responsive nanoplatform for enhancing combined chemo-photodynamic therapy, Adv. Mater. 29 (2017) 1605357.
[4] Z.M. Tang, D. Li, H.L. Sun, X. Guo, Y.P. Chen, S.B. Zhou, Quantitative control of active targeting of nanocarriers to tumor cells through optimization of folate ligand density, Biomaterials 35 (2014) 8015-8027.
[5] V.P. Torchilin, Recent approaches to intracellular delivery of drugs and DNA and organelle targeting, Annu. Rev. Biomed. Eng. 8 (2006) 343-375.
[6] Y. W. Won, K. S. Lim, Y. H. Kim, Intracellular organelle-targeted non-viral gene delivery systems. J. Control. Release 152 (2011) 99-109.
[7] Y. Wang, G.Q. Wei, X.B. Zhang, X.H. Huang, J.Y. Zhao, X. Guo, S.B. Zhou, Multistage targeting strategy using magnetic composite nanoparticles for synergism of photothermal therapy and chemotherapy, Small 14 (2018) 1702497.
[8] Y. Jing, X. Xiong, Y. Ming, J. Zhao, X. Guo, G. Yang, S. Zhou, A multifunctional micellar nanoplatform with pH-triggered cell penetration and nuclear targeting for effective cancer therapy and inhibition to lung metastasis, Adv. Healthc. Mater. 7 (2018) 1700974.
[9] L. Milane, M. Trivedi, A. Singh, M. Talekar, M. Amiji, Mitochondrial biology, targets, and drug delivery, J. Control. Release 207 (2015) 40-58.
[10] X. Guo, X. Wei, Y. Jing, S. Zhou, Size changeable nanocarriers with nuclear targeting for effectively overcoming multidrug resistance in cancer therapy, Adv. Mater. 27 (2015) 6450-6456.
[11] L. Li, W. Sun, J.J. Zhong, Q.Q. Yang, X. Zhu, Z. Zhou, Z.R. Zhang, Y. Huang, Multistage nanovehicle delivery system based on stepwise size reduction and charge reversal for programmed nuclear targeting of systemically administered anticancer drugs, Adv. Funct. Mater. 25 (2015) 4101-4113.
[12] K.A. Cimprich, D. Cortez, ATR: an essential regulator of genome integrity, Nat. rev. Mol. cell biol. 9 (2008) 616-627.
[13] P. Lu, B. J. Bruno, M. Rabenau, C. S. Lim, Delivery of drugs and macromolecules to the mitochondria for cancer therapy, J. Control. Release 240 (2016) 38-51.
[14] S. Fulda, L. Galluzzi, G. Kroemer, Targeting mitochondria for cancer therapy, Nat. rev. Drug disco. 9 (2010) 447-464.
[15] Q. Hu, M. Gao, G. Feng, B. Liu, Mitochondria-targeted cancer therapy using a light-up probe with aggregation-induced-emission characteristics, Angew. Chem. Int. Ed. 53 (2014) 14225-14229.
[16] S.R. Jean, M. Ahmed, E.K. Lei, S.P. Wisnovsky, S.O. Kelley, Peptide-mediated delivery of chemical probes and therapeutics to mitochondria, Acc. Chem. Res. 49 (2016) 1893-1902.
[17] L. Kazak, A. Reyes, I.J. Holt, Minimizing the damage: repair pathways keep mitochondrial DNA intact, Nat. rev. Mol. cell bio. 13 (2012) 659.
[18] E.A. Liberman, V.P. Topaly, L.M. Tsofina, A.A. Jasaitis, V.P. Skulachev, Mechanism of coupling of oxidative phosphorylation and the membrane potential of mitochondria, Nature 222 (1969) 1076-1078.

[19] J. Zielonka, J. Joseph, A. Sikora, M. Hardy, O. Ouari, J. Vasquez-Vivar, G. Cheng, M. Lopez, B. Kalyanaraman, Mitochondria-targeted triphenylphosphonium-based compounds: syntheses, mechanisms of action, and therapeutic and diagnostic applications, Chem. Rev. 117 (2017) 10043-10120.
[20] X.X. Wang, Y.B. Li, H.J. Yao, R.J. Ju, Y. Zhang, R.J. Li, Y. Yu, L. Zhang, W.L. Lu, The use of mitochondrial targeting resveratrol liposomes modified with a dequalinium polyethylene glycol-distearoylphosphatidyl ethanolamine conjugate to induce apoptosis in resistant lung cancer cells, Biomaterials 32 (2011) 5673-5687.
[21] L. Jiang, L. Li, X. He, Q. Yi, B. He, J. Cao, W. Pan, Z. Gu, Overcoming drug-resistant lung cancer by paclitaxel loaded dual-functional liposomes with mitochondria targeting and pH-response, Biomaterials 52 (2015) 126-139.
[22] J. Fernández-Carneado, M. Van Gool, V. Martos, S. Castel, P. Prados, J. de Mendoza, E. Giralt, Highly efficient, nonpeptidic oligoguanidinium vectors that selectively internalize into mitochondria, J. Am. Chem. Soc. 127 (2005) 869-874.
[23] A.E. Dikalova, A.T. Bikineyeva, K. Budzyn, R.R. Nazarewicz, L. McCann, W. Lewis, D.G. Harrison, S.I. Dikalov, Therapeutic targeting of mitochondrial superoxide in hypertension, Circ. Res. 107 (2010) 106-116.
[24] D.Y. Cho, H. Cho, K. Kwon, M. Yu, E. Lee, K.M. Huh, D.H. Lee, H.C. Kang, Triphenylphosphonium-conjugated poly (ε-caprolactone)-based self-assembled nanostructures as nanosized drugs and drug delivery carriers for mitochondria-targeting synergistic anticancer drug delivery, Adv. Funct. Mater. 25 (2015) 5479-5491.
[25] A.M. James, F.H. Blaikie, R.A. Smith, R.N. Lightowlers, P.M. Smith, M.P. Murphy, Specific targeting of a DNA-alkylating reagent to mitochondria: Synthesis and characterization of [4-((11aS)-7-methoxy-1, 2, 3, 11a-tetrahydro-5H-pyrrolo [2, 1-c][1, 4] benzodiazepine-5-on-8-oxy) butyl]-triphenylphosphonium iodide, Eur. J. Biochem. 270 (2003) 2827-2836.
[26] J.S. Modica-Napolitano, K.K. Singh, Mitochondrial dysfunction in cancer, Mitochondrion 4 (2004) 755-762.
[27] J.M. Adams, Ways of dying: multiple pathways to apoptosis, Genes Dev. 17 (2003) 2481-2495.
[28] Y. Li, X. Xu, X. Zhang, Y. Li, Z. Zhang, Z. Gu, Tumor-specific multiple stimuli-activated dendrimeric nanoassemblies with metabolic blockade surmount chemotherapy resistance, ACS Nano 11 (2017) 416-429.
[29] G. Masanta, C.S. Lim, H.J. Kim, J.H. Han, H.M. Kim, B.R. Cho, A mitochondrial-targeted two-photon probe for zinc ion, J. Am. Chem. Soc. 133 (2011) 5698-5700.
[30] H.S. Jung, J. Han, J.J. Lee, J.H. Lee, J.M. Choi, H.S. Kweon, J.H. Han, J.H. Kim, K.M. Byun, J.H. Jung, C. Kang, J.S. Kim, Enhanced NIR radiation-triggered hyperthermia by mitochondrial targeting, J. Am. Chem. Soc. 137 (2015) 3017-3023.
[31] M.F. Ross, G.F. Kelso, F.H. Blaikie, A.M. James, H.M. Cocheme, A. Filipovska, T. Da Ros, T.R. Hurd, R.A.J. Smith, M.P. Murphy, Lipophilic triphenylphosphonium cations as tools in mitochondrial bioenergetics and free radical biology, Biochemistry (Moscow) 70 (2005) 222-230.
[32] S.C. Ghosh, A.S. Neslihan, J. Klostergaard, CD44: a validated target for improved delivery of cancer therapeutics, Expert Opin. Ther. Targets 16 (2012) 635-650.
[33] Y.S. Liu, C.C. Chiu, H.Y. Chen, S.H. Chen, L.F. Wang, Preparation of chondroitin sulfate-g-poly (ε-caprolactone) copolymers as a CD44-targeted vehicle for enhanced intracellular uptake, Mol. Pharm. 11 (2014) 1164-1175.
[34] R. Bagari, D. Bansal, A. Gulbake, A. Jain, V. Soni, S.K. Jain, Chondroitin sulfate functionalized liposomes for solid tumor targeting, J. Drug Target. 19 (2011) 251-257.

[35] A. Pathak, P. Kumar, K. Chuttani, S. Jain, A. K. Mishra, S. P. Vyas, Gene expression, biodistribution, and pharmacoscintigraphic evaluation of chondroitin sulfate-PEI nanoconstructs mediated tumor gene therapy, ACS Nano 9 (2009) 2854-2854.
[36] A. Nakajima, K. Shinoda, Complex formation between oppositely charged polysaccharides. J. Colloid Interface Sci. 55 (1976) 126-132.
[37] N. Volpi, M. Dondi, A.M.F. Bolognani, Characterization of a small chondroitin sulfate proteoglycan isolated from the mucus surrounding the embryos of viviparus ater (mollusca gastropoda), Biochim. Biophys. Acta. 1380 (1998) 239-248.
[38] S. Zhou, X. Deng, H. Yang, Biodegradable copolymer of poly (ethylene glycol)-co-poly (ε-caprol actone): characterization and its use in controlled release system, Biomaterials 24 (2003) 3563-3570.
[39] J.Y. Zhu, Q. Lei, B. Yang, H.Z. Jia, W.X. Qiu, X. Wang, X. Zeng, R.X. Zhuo, J. Feng, X.Z. Zhang, Efficient nuclear drug translocation and improved drug efficacy mediated by acidity-responsive boronate-linked dextran/cholesterol nanoassembly, Biomaterials 52 (2015) 281-290.
[40] Y. Wang, L. Zhang, X. Zhang, X. Wei, Z. Tang, S. Zhou, Precise Polymerization of a Highly Tumor Microenvironment-Responsive Nanoplatform for Strongly Enhanced Intracellular Drug Release, ACS Appl. Mater. Interfaces 3 (2016) 5833-5846.
[41] J. Wang, G. Yang, X. Guo, Z. Tang, Z. Zhong, S. Zhou, Redox-responsive polyanhydride micelles for cancer therapy, Biomaterials 35 (2014) 3080-3090.
[42] C. Shi, X. Guo, Q. Qu, Z. Tang, Y. Wang, S. Zhou, Actively targeted delivery of anticancer drug to tumor cells by redox-responsive star-shaped micelles, Biomaterials 35 (2014) 8711-8722.
[43] G.K. Such, Y. Yan, A.P. Johnston, S.T. Gunawan, F. Caruso, Interfacing materials science and biology for drug carrier design, Adv. Mater. 27 (2015) 2278-2297.
[44] Q. Qu, Y. Wang, L. Zhang, X. Zhang, S. Zhou, A Nanoplatform with precise control over release of cargo for enhanced cancer therapy, Small 12 (2016) 1378-1390.
[45] X. Guo, C.L. Shi, G. Yang, J. Wang, Z.H. Cai, S.B. Zhou, Dual-responsive polymer micelles for target-cell-specific anticancer drug delivery, Chem. Mater. 26 (2014) 4405-4418.
[46] Y.W. Hu, Y.Z. Du, N. Liu, X. Liu, T.T. Meng, B.L. Cheng, J.B. He, J. You, H. Yuan, F.Q. Hu, Selective redox-responsive drug release in tumor cells mediated by chitosan based glycolipid-like nanocarrier, J. Control. Release 206 (2015) 91-100.
[47] V. Zinchuk, O. Grossenbacher-Zinchuk, Recent advances in quantitative colocalization analysis: Focus on neuroscience, Prog. Histochem. Cytochem. 44 (2009) 125-172.
[48] A. Cossarizza, M. Baccaranicontri, G. Kalashnikova, C. Franceschi, A new method for the cytofluorometric analysis of mitochondrial membrane potential using the J-aggregate forming lipophilic cation 5,5',6,6'-tetrachloro-1,1',3,3'-tetraethylbenzimidazolcarbocyanine iodide (JC-1), Biochem. Biophys. Res. Commun. 197 (1993) 40-45.
[49] S.W. Perry, J.P. Norman, J. Barbieri, E.B. Brown, H.A. Gelbard, Mitochondrial membrane potential probes and the proton gradient: a practical usage guide, Biotechniques 50 (2011) 98-115.
[50] M. Okada, N.I. Smith, A.F. Palonpon, H. Endo, S. Kawata, M. Sodeoka, K. Fujita, Label-free Raman observation of cytochrome c dynamics during apoptosis, Proc. Natl. Acad. Sci. USA 109 (2012) 28-32.
[51] M.L. Boland, A.H. Chourasia, K.F. Macleod, Mitochondrial dysfunction in cancer, Front. Oncol. 3 (2013) 292.
[52] D.M. Hockenbery, Targeting mitochondria for cancer therapy, Environ. Mol. Mutagen. 51 (2010) 476-489.
[53] H.L. Tu, Y.S. Lin, H.Y. Lin, Y. Hung, L.W. Lo, Y.F. Chen, C.Y. Mou, In vitro studies of functionalized mesoporous silica nanoparticles for photodynamic therapy, Adv. Mater. 21 (2009) 172-177.

[54] J. Xu, F. Zeng, H. Wu, C. Hu, C. Yu, S. Wu, Preparation of a mitochondria-targeted and NO-releasing nanoplatform and its enhanced pro-apoptotic effect on cancer cells, Small 10 (2014) 3750-3760.

Figure captions

Scheme 1. A) Formation of the micelles by the self-assembly of TPP-PEG-ss-PLA polymer and subsequently coated with CS layer, and the disassembly of the nanoparticle via the initial deshielding of CS layer by pH-response followed by the cleavage of the disulfide bonds by GSH response. **B**) Schematic illustration of the stepwise dual targeting and dual response of the micelles to induce apoptosis of tumor cells. 1) Increased endocytosis through receptor-mediated cell membrane targeting; 2) Mitochondrial targeting via TPP exposure due to pH response, which causes decreases in the membrane potential (ΔΨm) and overproduction of the ROS and finally leads to cell apoptosis; 3) The DOX released due to the disassembly by GSH response diffuses to the mitochondria and the nucleus and damages DNA. **C**) Magnification of the series process including mitochondrial targeting, decreases in the membrane potential (ΔΨm), overproduction of the ROS, and drug diffusion into the mitochondria.

Figure 1. Determination of the pH and reduction in the sensitivity of the micelles. Transmission electron microscopy (TEM) images and changes in the size of corresponding nanoparticles: **A-B**) TPP-PEG-ss-PLA; **C-D**) CS/TPP-PEG-ss-PLA; **E-F**) Morphology and size changes for CS/TPP-PEG-ss-PLA nanoparticles in 10 mM GSH at pH 7.4; **G-H**) Determination of pH sensitivity of the CS/TPP-PEG-ss-PLA nanoparticles for different pH values and times (indicates ± standard deviation (SD), n = 3); **I**) *In vitro* DOX release profiles (indicates ± SD, n = 3).

Figure 2. Mitochondria-targeting analysis. **A**) CLSM images for tracking DOX delivery in HepG2 cells with MitoTracker-stained mitochondrion channel (green) or DOX channel (red). **B, C**) Co-localization analysis.

Figure 3. *In vitro* Analyses of the mitochondrial membrane potential and ROS generation. **A**) JC-1 staining in HepG2 cells via treatment with different micelles for 6 h. **B**) Flow cytometric analyses of mitochondrial membrane potential using JC-1 as indicator for HepG2 cells treated with various micelles at different concentrations for 6 h and 12 h. Relative intensity of JC-1 red fluorescence for **C**) 6 h and **D**) 12 h (indicates ± SD, n = 3). **E**) DCFH-DA staining in HepG2 cells after treatment with different micelles for 6 h. **F**) Relative intensity of DCFH-DA green fluorescence. **G**) Mean fluorescence intensity (MFI) of the DCFH-DA staining in HepG2 cells after treatment with CS/TPP-PEG-ss-PLA at different concentrations (indicates ± SD, n = 3). **H**) Viability of HepG2 cells following incubation with free DOX and DOX-loaded corresponding nanoparticles (indicates ± SD, n = 3).

Figure 4. *In vivo* analysis of mitochondrial membrane potential and ROS generation. Two-photon laser confocal fluorescence microscopy images of **A**) in vivo JC-1 staining and **B**) DCFH-DA staining on Balb/c mice bearing H22 tumor following treatment with different micelles for 24 h. **C**) Relative intensity of DCFH-DA fluorescence from green.

Figure 5. *In vivo* and *ex vivo* biodistribution analyses. **A**) *In vivo* fluorescence images of H22 tumor bearing nude mice following intravenous injection of various DOX formulations and *ex vivo* fluorescence images of isolated tissues at 6 h post-injection. **B**) Pharmacokinetic profiles of total DOX, post-intravenous injection of various DOX formulations (indicates ± SD, n = 3). **C-H**) DOX distribution in the tumor, heart, liver, spleen, lung, and kidneys (n = 3) (dose: 2 mg DOX/kg body weight, indicates ± SD, $^{**}P < 0.01$).

Figure 6. *In vivo* antitumor activity evaluation. **A**) Changes in the tumor volume and **B**) Monitored tumor size of Balb/c mice bearing H22 tumor following intravenous saline injection, DOX·HCl, and corresponding nanoparticles (2.0 mg DOX/kg body weight, indicates ± SD, n = 7), **C**) Body weight, **D**) Tumor growth inhibition, **E**) TUNEL and H&E analyses of tumor sections after treatment. In TUNEL staining, normal cells are stained blue, and apoptotic cells are stained brown. In H&E staining, nuclei are stained blue, and the extracellular matrix and cytoplasm are stained red. (**P < 0.01 and ***P < 0.001)

Graphical abstract

Highlights:

- The nanocarriers have a long blood circulation time due to the negative charged surface and enhanced internalization of tumor cells.
- The micelles can target and anchor into mitochondrial outer membrane, thereby inducing the depolarization of mitochondrial membrane.
- The released DOX can directly diffuse into the mitochondria, thereby resulting in mitochondrial DNA damage.

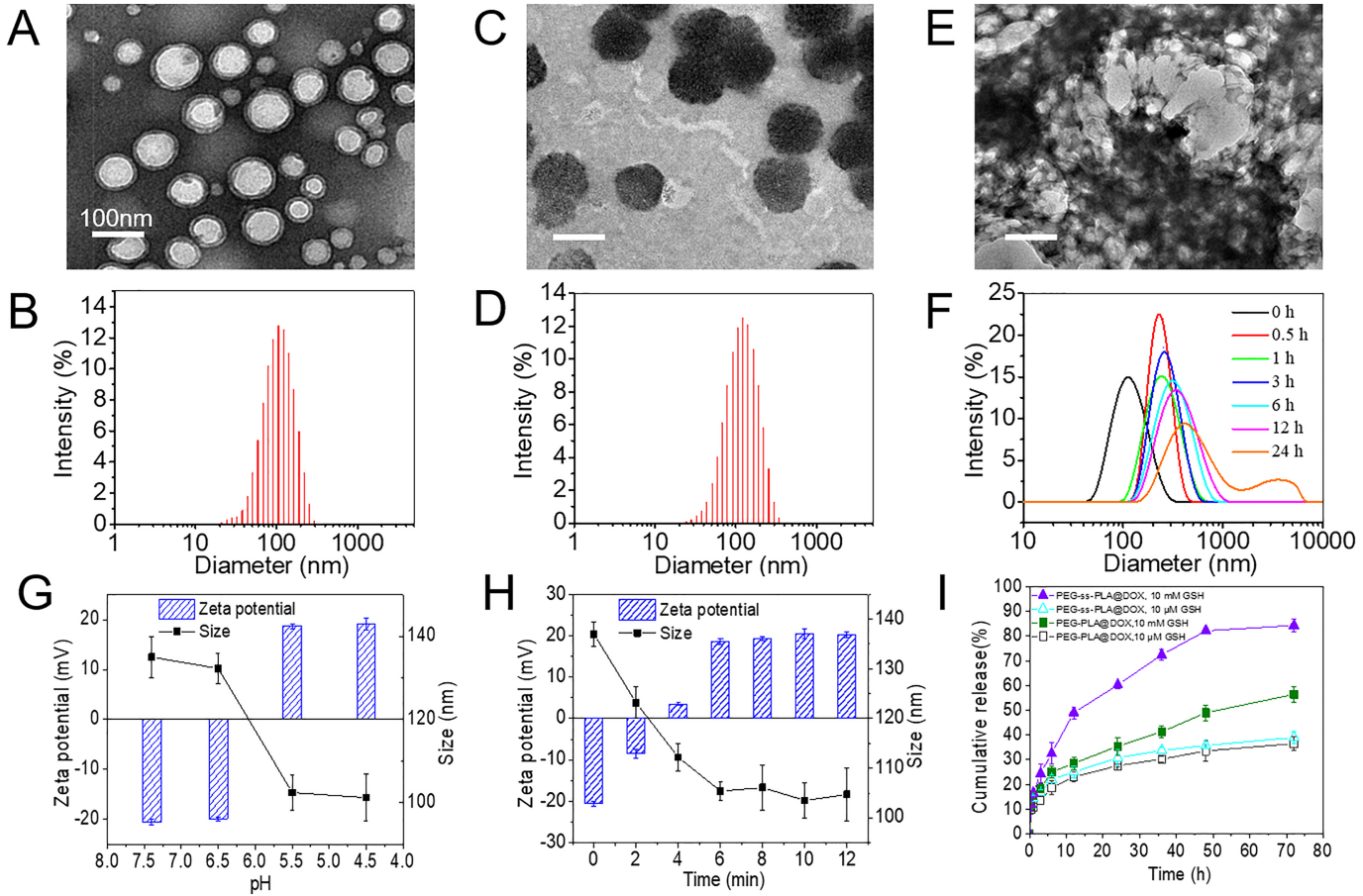
A
100nm
C
E
B
Intensity (%)
Diameter (nm)
D
Intensity (%)
Diameter (nm)
F
Intensity (%)
0 h
0.5 h
1 h
3 h
6 h
12 h
24 h
Diameter (nm)
G
Zeta potential
Size
Zeta potential (mV)
Size (nm)
pH
H
Zeta potential
Size
Zeta potential (mV)
Size (nm)
Time (min)
I
PEG-ss-PLA@DOX, 10 mM GSH
PEG-ss-PLA@DOX, 10 μM GSH
PEG-PLA@DOX,10 mM GSH
PEG-PLA@DOX,10 μM GSH
Cumulative release(%)
Time (h)

Figure 1

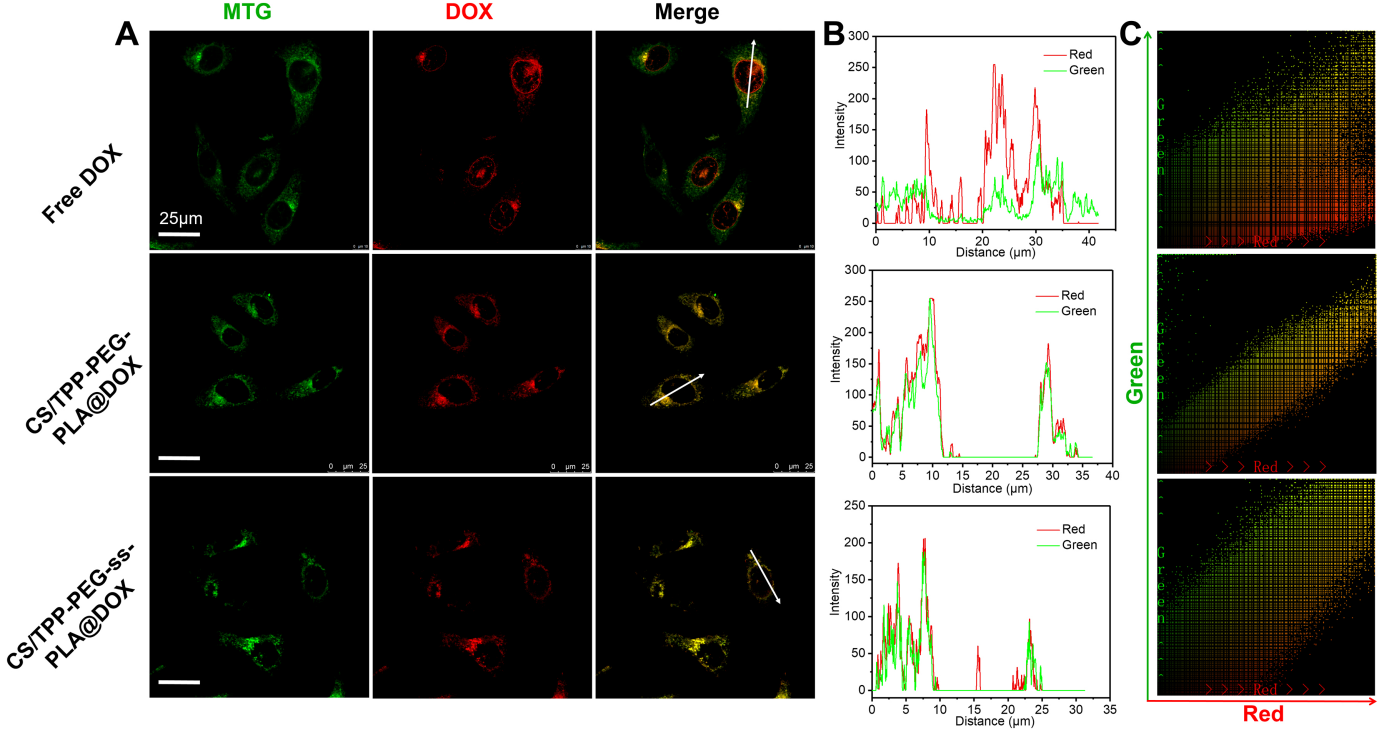
A
MTG
DOX
Merge
Free DOX
CS/TPP-PEG-PLA@DOX
CS/TPP-PEG-ss-PLA@DOX
25μm
B
Red
Green
Intensity
Distance (μm)
C
Green
Red

Figure 2

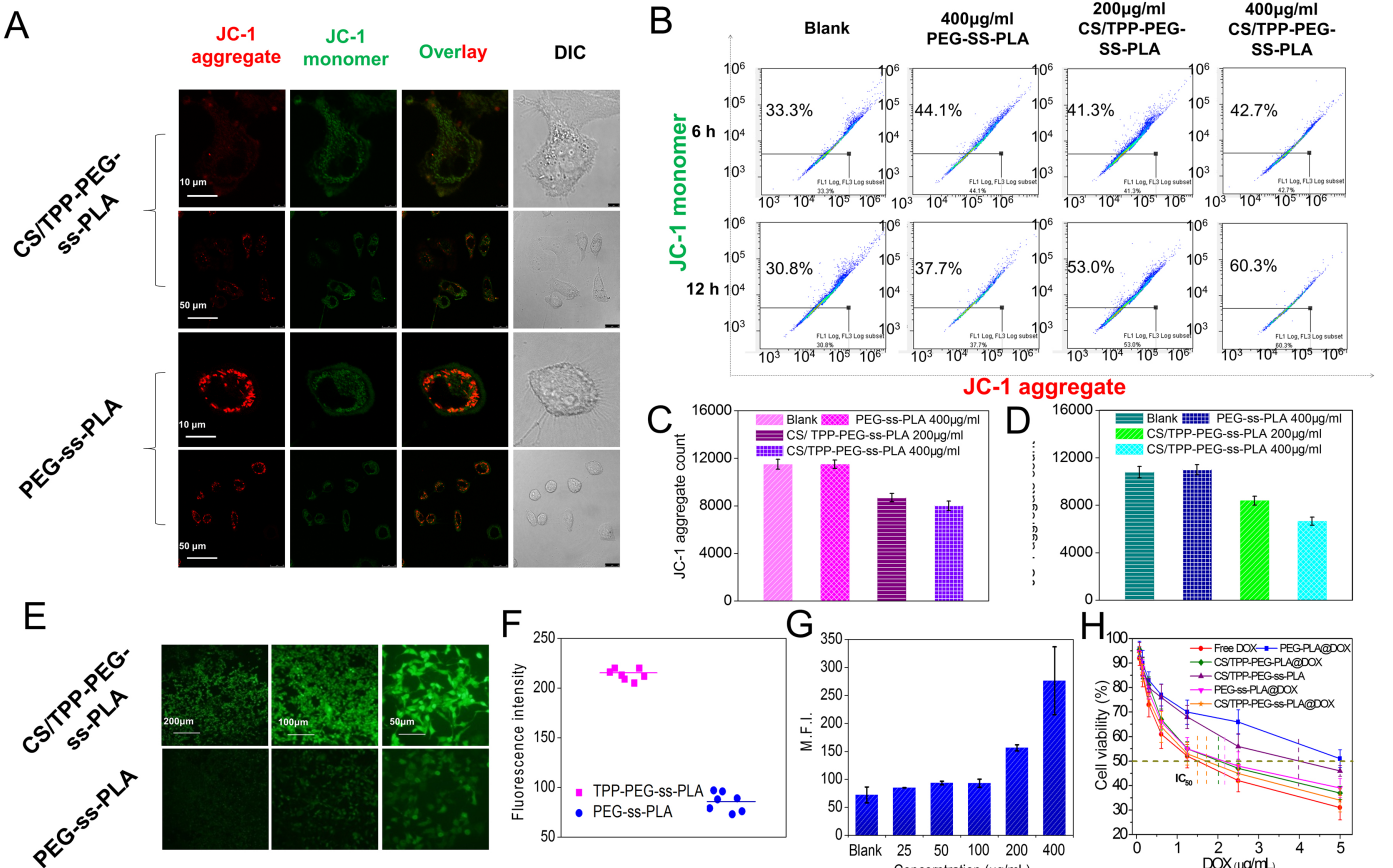
A
JC-1 aggregate
JC-1 monomer
Overlay
DIC
CS/TPP-PEG-ss-PLA
PEG-ss-PLA
10 μm
50 μm
B
Blank
400μg/ml PEG-SS-PLA
200μg/ml CS/TPP-PEG-SS-PLA
400μg/ml CS/TPP-PEG-SS-PLA
JC-1 monomer
6 h
12 h
33.3%
44.1%
41.3%
42.7%
30.8%
37.7%
53.0%
60.3%
JC-1 aggregate
C
JC-1 aggregate count
Blank
PEG-ss-PLA 400μg/ml
CS/ TPP-PEG-ss-PLA 200μg/ml
CS/TPP-PEG-ss-PLA 400μg/ml
D
CS/TPP-PEG-ss-PLA 200μg/ml
E
200μm
100μm
50μm
F
Fluorescence intensity
TPP-PEG-ss-PLA
PEG-ss-PLA
G
M.F.I.
Blank
25
50
100
200
400
Concentration (μg/mL)
H
Free DOX
PEG-PLA@DOX
CS/TPP-PEG-PLA@DOX
CS/TPP-PEG-ss-PLA
PEG-ss-PLA@DOX
CS/TPP-PEG-ss-PLA@DOX
Cell viability (%)
IC50
DOX (μg/mL)

Figure 3

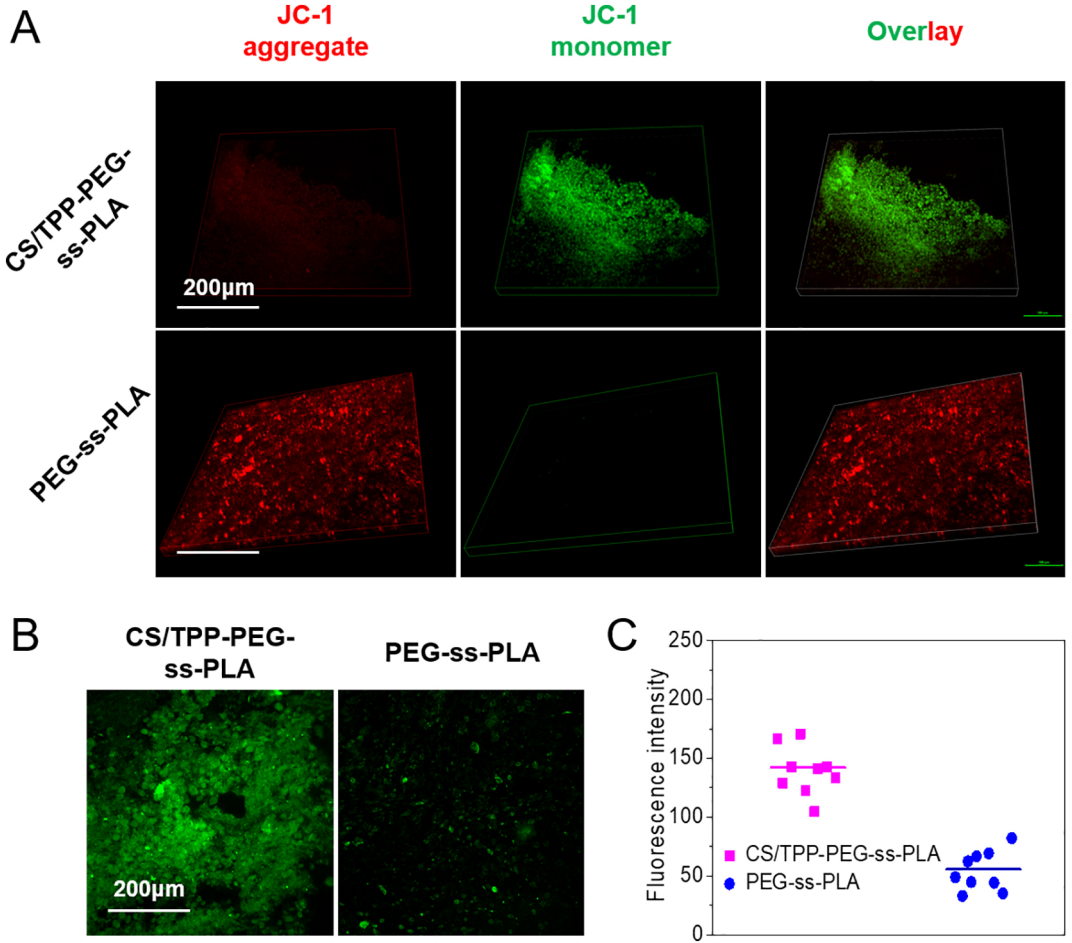
A
JC-1 aggregate
JC-1 monomer
Overlay
CS/TPP-PEG-ss-PLA
PEG-ss-PLA
200μm
B
CS/TPP-PEG-ss-PLA
PEG-ss-PLA
200μm
C
Fluorescence intensity
250
200
150
100
50
0
CS/TPP-PEG-ss-PLA
PEG-ss-PLA

Figure 4

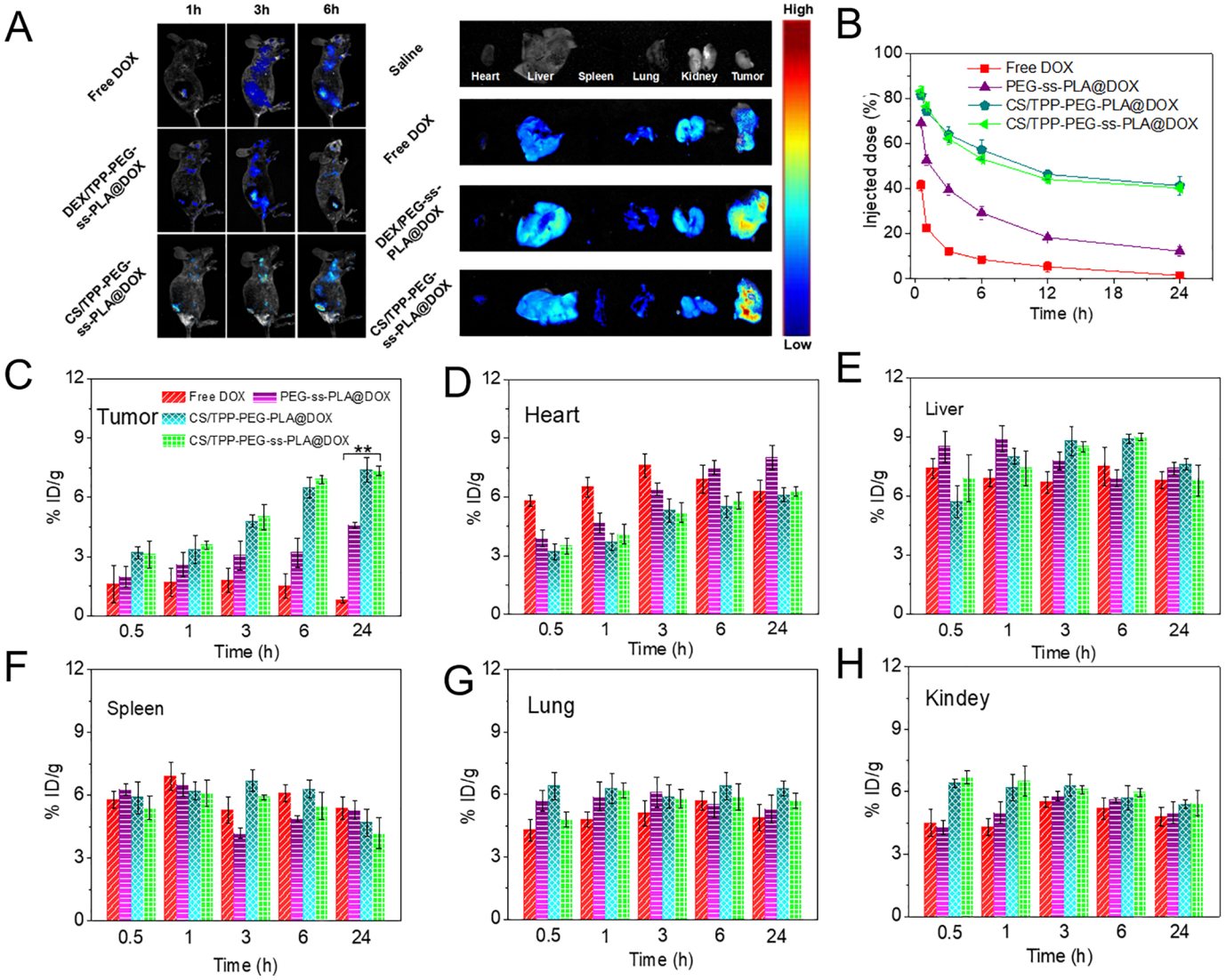
A
1h
3h
6h
Free DOX
DEX/TPP-PEG-ss-PLA@DOX
CS/TPP-PEG-ss-PLA@DOX
Saline
Free DOX
DEX/PEG-ss-PLA@DOX
CS/TPP-PEG-ss-PLA@DOX
Heart
Liver
Spleen
Lung
Kidney
Tumor
High
Low
B
Free DOX
PEG-ss-PLA@DOX
CS/TPP-PEG-PLA@DOX
CS/TPP-PEG-ss-PLA@DOX
Injected dose (%)
Time (h)
C
Tumor
Free DOX
PEG-ss-PLA@DOX
CS/TPP-PEG-PLA@DOX
CS/TPP-PEG-ss-PLA@DOX
**
% ID/g
Time (h)
D
Heart
E
Liver
F
Spleen
G
Lung
H
Kindey

Figure 5

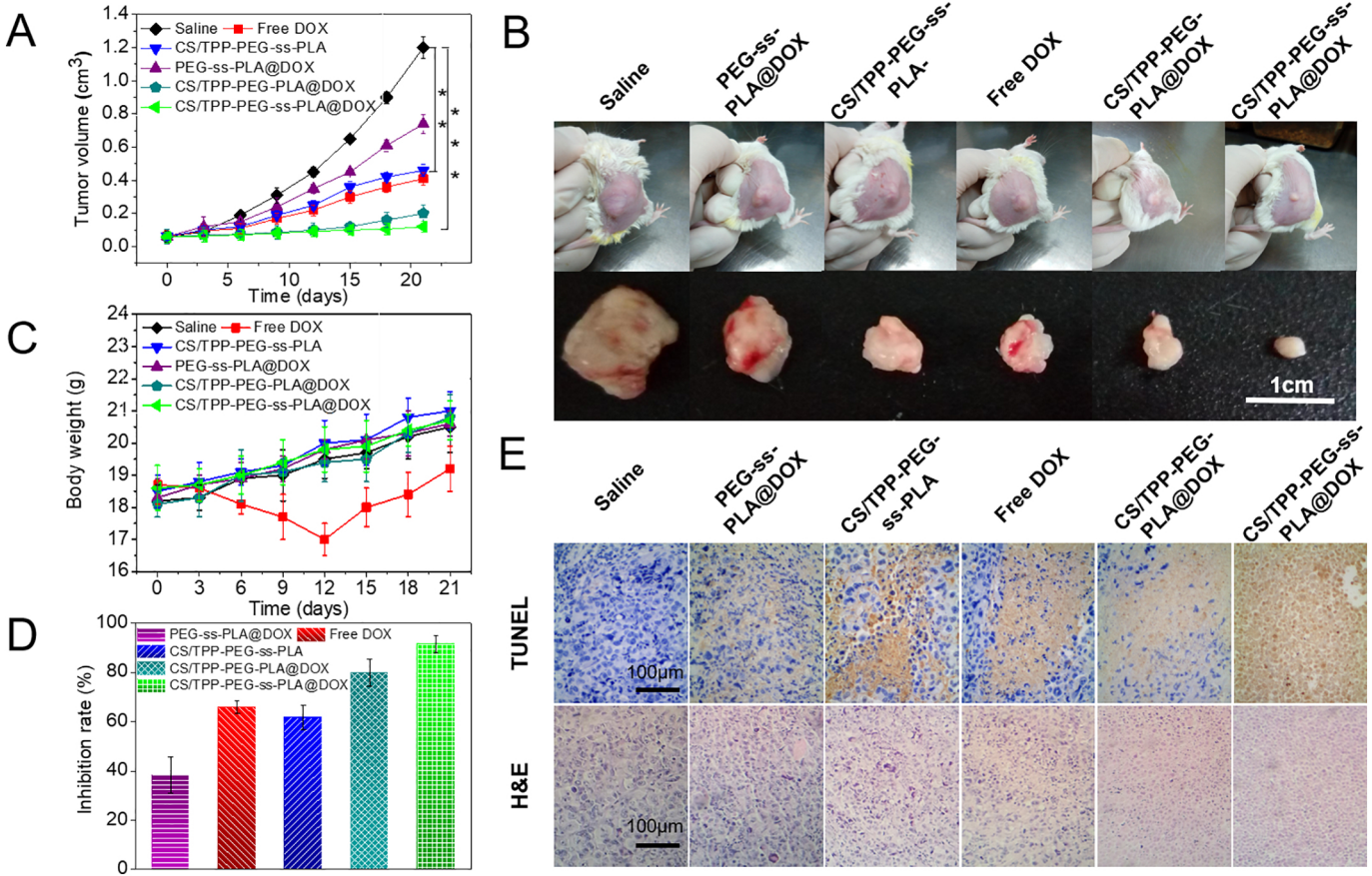
A
Tumor volume (cm3)
Time (days)
Saline
Free DOX
CS/TPP-PEG-ss-PLA
PEG-ss-PLA@DOX
CS/TPP-PEG-PLA@DOX
CS/TPP-PEG-ss-PLA@DOX
B
Saline
PEG-ss-PLA@DOX
CS/TPP-PEG-ss-PLA-
Free DOX
CS/TPP-PEG-PLA@DOX
CS/TPP-PEG-ss-PLA@DOX
1cm
C
Body weight (g)
Time (days)
D
Inhibition rate (%)
E
TUNEL
H&E
100μm

Figure 6